RSC Advances

PAPER

View Article Online
View Journal | View Issue

Cite this: *RSC Adv.*, 2026, **16**, 23136

Sunlight-driven fast photo-degradation of Eriochrome Black T dye using highly efficient La-doped Ag_3PO_4 decorated with ZnS QDs

Shabana Bibi,[a] Amna Bashir,[b] Noshabah Tabassum,[a] It Ee Lee,*[cd] Hafsa Yasmeen,[b] Syed Mustansar Abbas,[f] Qamar Wali,[cd] Muhammad Aamir,[e] Chingmai Ko[g] and Imtiaz Ahmad *[g]

The untreated discharge of dye-contaminated effluents into aquatic environments poses serious risks to both environmental integrity and public health. Therefore, the development of efficient dye removal strategies is essential for pollution control and ecosystem protection. This study aims to investigate and optimize the photocatalytic degradation of Eriochrome Black T (EBT) in aqueous solutions using novel Ag_3PO_4-based composites, including lanthanum-doped Ag_3PO_4, and ZnS quantum dots under sunlight irradiation. Pure Ag_3PO_4, 2% and 6% La-doped Ag_3PO_4, and ZnS quantum dots were synthesized *via* a co-precipitation method, and their composite photocatalysts were fabricated using a hybrid mixing approach. The characterizations of the materials were carried out using X-ray diffraction, BET surface area analysis, UV-visible diffuse reflectance spectroscopy (UV-vis DRS), Fourier transform infrared (FTIR) spectroscopy, Raman spectroscopy, X-ray photoelectron spectroscopy (XPS), thermogravimetric analysis (TGA), and scanning electron microscopy with energy-dispersive spectroscopy (SEM–EDS) to evaluate their structural, optical, and morphological properties. The synthesized photocatalysts, including pure Ag_3PO_4, 2% and 6% La-doped Ag_3PO_4, ZnS quantum dots, and their composite systems, exhibited well-defined crystalline structures, as confirmed by X-ray diffraction (XRD) analysis. UV-vis DRS analysis showed that pure Ag_3PO_4 had a band gap of 2.41 eV, which decreased to 2.39 eV for 2% La-doped Ag_3PO_4 and 2.36 eV for 6% La-doped Ag_3PO_4, while ZnS quantum dots exhibited a band gap of 3.6 eV, and the 6% La-doped Ag_3PO_4/ZnS QD composite showed a significantly reduced band gap of 1.5 eV. Upon the incorporation of ZnS QDs into the 6% La-Ag_3PO_4 particles, the surface area of the 6% La-Ag_3PO_4 heterojunction composite increased from 133.446 to 141.120 $m^2\ g^{-1}$. The photocatalytic activity of the synthesized Ag_3PO_4-based materials was evaluated through the degradation of Eriochrome Black T (EBT) under light irradiation. The influence of key operational parameters, including the solution pH (3–10), dye concentration (10–20 ppm), photocatalyst dosage (0.05–0.15 g), and irradiation time (5–120 min), was systematically investigated to assess their effect on degradation efficiency. Among the examined photocatalysts, 6% La-doped Ag_3PO_4 exhibited the highest photocatalytic performance, demonstrating the beneficial role of lanthanum incorporation. The degradation efficiencies of 97.84% and 84.88% were achieved using 6% La-doped Ag_3PO_4 and the 6% La-doped Ag_3PO_4/ZnS QD composite, respectively, under the optimized conditions of pH 6 and an irradiation time of 120 min. Overall, these results indicate that La-modified Ag_3PO_4-based photocatalysts are promising and sustainable materials for the effective treatment of dye-contaminated wastewater, offering significant potential for environmental remediation applications.

Received 21st January 2026
Accepted 13th April 2026

DOI: 10.1039/d6ra00544f

rsc.li/rsc-advances

[a]*Department of Environment Sciences, Fatima Jinnah Women University, The Mall, Rawalpindi, 46000, Pakistan*

[b]*Department of Chemistry, Fatima Jinnah Women University, The Mall, Rawalpindi, 46000, Pakistan. E-mail: amnabashir79@yahoo.com*

[c]*Faculty of Artificial Intelligence and Engineering, Multimedia University, 63100 Cyberjaya, Malaysia. E-mail: ielee@mmu.edu.my*

[d]*Centre for Smart Systems and Automation, COE for Robotics and Sensing Technologies, Multimedia University, 63100 Cyberjaya, Selangor, Malaysia*

[e]*Department of Chemistry, Mirpur University of Science and Technology (MUST), Mirpur-10250 (AJK), Pakistan*

[f]*Department of Chemistry, College of Science, Imam Abdulrahman Bin Faisal University, P.O. Box 1982, Dammam, Saudi Arabia*

[g]*School of Electronics and Communication Engineering, Quanzhou University of Information Engineering, Quanzhou, 362000, China*

1 Introduction

Rapid population growth and ongoing industrial development are major contributors to water pollution, creating serious environmental, economic, and public health challenges by contaminating vital water resources.[1–4] Organic substances like dyes and hazardous pollutants like heavy metals are the main sources of water contamination.[5,6] Azo dyes, commonly applied in textile industries, are a significant source of water pollution. These dyes are extremely resistant to degradation, even under sunlight, with half-lives exceeding two thousand hours.[7] More than 50% of the dye produced worldwide is Eriochrome Black T (EBT).[8–10] Many industries, including pharmaceutical, paper printing, leather, paint, and cosmetics, utilize it, which contaminates the water.[11] Its intricate chemical structure, resistance to photodegradation, and light stability make it a significant target for removal.[12–14]

Indiscriminate effluent discharge from industries is largely responsible for the rise in water pollution, causing rapid deterioration in water quality and posing serious environmental threats. Pollutants like EBT accumulate in different parts of plants or plant products, which are then consumed by humans and animals, entering the food chain and having negative effects. Additionally, groundwater may become contaminated by EBT-containing industrial effluents, rendering it unsafe for human consumption.[15–18] Numerous health problems, such as pulmonary toxicity, genetic lesions, genetic mutation, congenital malformations, and oncogenesis, can result from long-term exposure to high concentrations of EBT dye.[19,20] For this reason, wastewater must be properly treated before being released into the environment. It is also vital to develop affordable, efficient, and eco-friendly technology for removing EBT and azo dyes from both water and wastewater sources.

All dyes, especially reactive dyes, cannot always be completely removed using conventional dye removal techniques, which include physical and biological processes. Photocatalysis is one of the most promising processes (AOPs) which helps in the oxidative elimination of organic contaminants. The breakdown of organic pollutants is accelerated by this process, which uses catalysts and light sources. Studies reveal that the pigments in industrial effluents can be removed by photocatalysis at a rate of 70–80%. In an effort to achieve efficient dye degradation, numerous scientists are studying heterogeneous photocatalysts, including WO_3, ZnO, and TiO_2.[21]

Ag_3PO_4 has been synthesized in various shapes as reported in literature such as tetrapod, tetrahedral, cubic, spherical, and trisoctahedral.[22–25] When exposed to visible light, the produced Ag_3PO_4 showed 100% photodegradation of the MB dye. Concave trioctahedral Ag_3PO_4 particles were created. using the same process but with a different phosphate precursor. Furthermore, when employed as a photocatalyst for the degradation of RhB dye, they similarly achieved 100% degradation under visible-light illumination.[23] Many studies have shown that silver phosphate displays excellent photocatalytic performance. However, it also has a high photogenerated charge-carrier recombination rate. Therefore, doping has been incorporated into the host Ag_3PO_4's lattice site to increase its photocatalytic potential. Dopants such as nickel, bismuth, lanthanum, fluorine, sulfate, carbonate, and rare-earth elements (dysprosium, erbium, and gadolinium) have been identified in several studies. These elements have the potential to enhance the chemical characteristics and photocatalytic efficiency of Ag_3PO_4.[26–32] It has also been reported that lanthanum, as a dopant, alters the surface structure of the host lattice.[33,34] Amirulsyafiee *et al.* used the coprecipitation method to synthesize La-doped Ag_3PO_4 and studied its photocatalytic performance under visible light. The 1% La-doped Ag_3PO_4 demonstrated superior photocatalytic activity, degrading 81% of methylene blue in 60 minutes and 94% of methyl orange in 30 minutes. The enhanced photocatalytic efficiency was attributed to reduced electron–hole recombination and morphological changes resulting from lanthanum incorporation.[32,35] Ag_3PO_4 suffers from photocorrosion due to Ag^+ reduction under visible light. Therefore, La^{3+} doping confers Ag_3PO_4 anti-photocorrosion properties by altering internal electron migration pathways, introducing new electronic states, and improving electron migration, thereby enhancing charge separation, facilitating internal electron transfer, and increasing photocatalytic stability.[36]

Zinc sulfide (ZnS) is one of the most attractive metal chalcogenides due to its intrinsic properties, including high electronic mobility, water insolubility, low cost, and non-toxicity.[37,38] ZnS QDs have been modified for increased photocatalytic effectiveness using techniques such as heterojunction creation and dopant inclusion.[39] Recent studies have revealed that tuning the electronic structure and coordination environment of catalysts is an effective strategy to enhance charge separation and improve photocatalytic efficiency.[40] Furthermore, the construction of heterojunction systems has been widely explored to promote interfacial charge transfer and extend light absorption. In addition, the local structural distortion of catalytic sites can regulate electron density and facilitate charge transfer, which plays a crucial role in determining catalytic performance.[41] The photocatalytic activity of a material is also strongly influenced by its band gap. An effective photocatalyst typically has a band gap in the range of 2–3 eV, allowing efficient visible-light absorption while providing sufficient redox potential for photocatalytic reactions, whereas materials with too low a band gap (<1.23 eV) are generally not suitable, as they cannot facilitate the necessary redox processes effectively.[42]

In the current work, Ag_3PO_4, La-doped Ag_3PO_4, and ZnS QDs were synthesized *via* a co-precipitation method. The composites were formed by mixing. The photocatalytic performance of individual components and the composites was studied for the degradation of Eriochrome Black T (EBT) under sunlight irradiation. Comprehensive characterizations of the synthesized materials were carried out using X-ray diffraction, BET surface area analysis, UV-visible diffuse reflectance spectroscopy (UV-vis DRS), Fourier transform infrared (FTIR) spectroscopy, Raman spectroscopy, X-ray photoelectron spectroscopy (XPS), thermogravimetric analysis (TGA), and scanning electron microscopy with energy-dispersive spectroscopy (SEM–EDS) to evaluate their structural, optical, and morphological properties. The influence of key factors, including the dye concentration,

catalyst dose, pH, and temperature, was thoroughly investigated. Interestingly, the individual components exhibited higher degradation efficiency for EBT dye than the composites under the conditions studied. No studies are available on undoped Ag_3PO_4 and doped Ag_3PO_4 for EBT degradation. Furthermore, the ZnS quantum dots synthesized *via* the presented co-precipitation approach have not been explored for EBT degradation. However, direct comparison with previously reported studies is limited, as, to the best of our knowledge, Ag_3PO_4-based photocatalysts have not been explored for EBT degradation. Therefore, this study not only introduces a new photocatalytic system but also extends the application of Ag_3PO_4-based materials to a previously unexplored EBT azo dye, providing new insights into their photocatalytic behaviour.

2 Materials and methods

The chemicals used for synthesis in this research were silver nitrate ($AgNO_3$; Sigma-Aldrich), potassium dihydrogen phosphate (KH_2PO_4; Scharlau), lanthanum nitrate hexahydrate ($La(NO_3)_3 \cdot 6H_2O$; Sigma-Aldrich), zinc acetate dihydrate ($Zn(CH_3COO)_2 \cdot 2H_2O$; Scharlau), sodium sulfide (Na_2S; Sigma-Aldrich), sodium dodecyl sulfate (Sigma-Aldrich), deionized water, distilled water, and Eriochrome Black T (Sigma-Aldrich).

2.1 Synthesis of Ag_3PO_4 and La-doped Ag_3PO_4

Silver phosphate (Ag_3PO_4) and lanthanum-doped silver phosphate (La-Ag_3PO_4) were synthesized *via* a modified co-precipitation method.[35] Briefly, 0.1 M $AgNO_3$ and 0.3 M KH_2PO_4 solutions were prepared separately in 20 mL of deionized water. The KH_2PO_4 solution was added dropwise to the $AgNO_3$ solution under continuous stirring, resulting in the formation of yellow precipitates (confirming the formation of Ag_3PO_4). The suspension was left undisturbed for 2 hours to allow the precipitates to settle, followed by vacuum filtration and repeated washing with deionized water. The obtained product was dried in an oven for 2 hours and stored.

For La-doped Ag_3PO_4 synthesis, the same procedure was followed with the addition of an appropriate amount of $La(NO_3)_3 \cdot 6H_2O$ to the $AgNO_3$ solution to achieve 2% and 6% La doping. The schematic representation of the synthesis route of Ag_3PO_4 and La-doped Ag_3PO_4 is shown in Fig. 1(a).

2.2 Synthesis of ZnS quantum dots

The co-precipitation method was used to synthesize ZnS quantum dots with slight modifications.[43] In the standard synthesis procedure, a 0.5 M zinc acetate dihydrate solution and a 0.5 M sodium sulfide solution were prepared in 25 mL of distilled water. Then, the zinc acetate solution was added to the sodium sulfide solution dropwise under constant stirring at neutral pH. Additionally, 25 mL of a 0.5 M SDS solution was added dropwise to the solution while being constantly stirred. The above solution was stirred for 2 hours until white precipitates were formed. The solution was filtered and washed with a mixture of water and ethanol several times. The precipitates were dried in an oven at 60 °C for 5 hours. In Fig. 1(b), a schematic of the synthesis of ZnS quantum dots is presented.

2.3 Synthesis of composites

The Ag_3PO_4/ZnS composite was prepared by combining Ag_3PO_4 and ZnS quantum dots in a 1 : 1 weight ratio. In the typical process, 0.5 g of the synthesized Ag_3PO_4 was dispersed in 25 mL of deionized water and ultrasonicated at 30 °C for 15 minutes. Subsequently, 0.5 g of ZnS quantum dots was added to the mixture, followed by ultrasonication for 15 min to achieve uniform dispersion. The mixture was then stirred for 2 hours, during which dark-green precipitates formed, indicating the formation of the Ag_3PO_4/ZnS composite. The product was allowed to settle, filtered, washed several times with deionized water, and dried in an oven for 2 hours at 50–60 °C. Fig. 1(c) presents the schematic illustration of the synthesis method of Ag_3PO_4/ZnS QDs and La-doped Ag_3PO_4/ZnS QDs. The synthesis of La-Ag_3PO_4/ZnS composites followed the same procedure, using La-doped Ag_3PO_4 (2% and 6%) instead of pure Ag_3PO_4.

The crystal structure and crystalline size of the synthesized materials were analysed using XRD. FTIR spectroscopy was utilized to examine the functional groups of the synthesized materials. An FTIR spectrophotometer (SHIMADZU-8400) was used to record FTIR spectra in the range from 400 to 4000 cm^{-1}. The surface morphology of the synthesized materials was analysed by scanning electron microscopy (SEM). The elemental composition of the synthesized materials was determined using energy-dispersive X-ray spectroscopy (EDS). The thermal behaviour of the synthesized materials was analysed by thermogravimetric analysis (TGA) in an inert gas atmosphere. Raman spectroscopy was used to investigate the structural and vibrational properties of the synthesized materials.

2.4 Adsorption experiments

The adsorption studies were conducted using a method already reported in the literature, with slight modifications.[44] Briefly, an adsorption experiment was conducted using a 15 ppm dye solution at 25 °C. An appropriate quantity of the catalyst (0.1 g) and 50 mL of the dye solution were combined, and the mixture was stirred for 1 hour in the dark. After 1 hour, an aliquot of the solution was taken out, followed by the separation of the catalyst by centrifugation. The absorbance was measured at 550 nm using a UV-visible spectrophotometer. Fig. S1(a) presents the schematic representation of the adsorption experiment.

2.5 Photocatalytic degradation experiments

The photocatalytic degradation experiment was conducted in direct sunlight using a previously reported method.[45,46] Briefly, a known quantity of the catalyst (0.1 g) was added to 50 mL of a dye solution. The dye solution was exposed to direct sunlight for 2 hours under continuous stirring. An adequate volume of the solution was removed after 5, 15, 30, 45, 60, and 120 min. The catalyst was removed from the sample *via* centrifugation, and the absorbance was measured at 550 nm. The schematic representation of the photocatalytic experiment is shown in

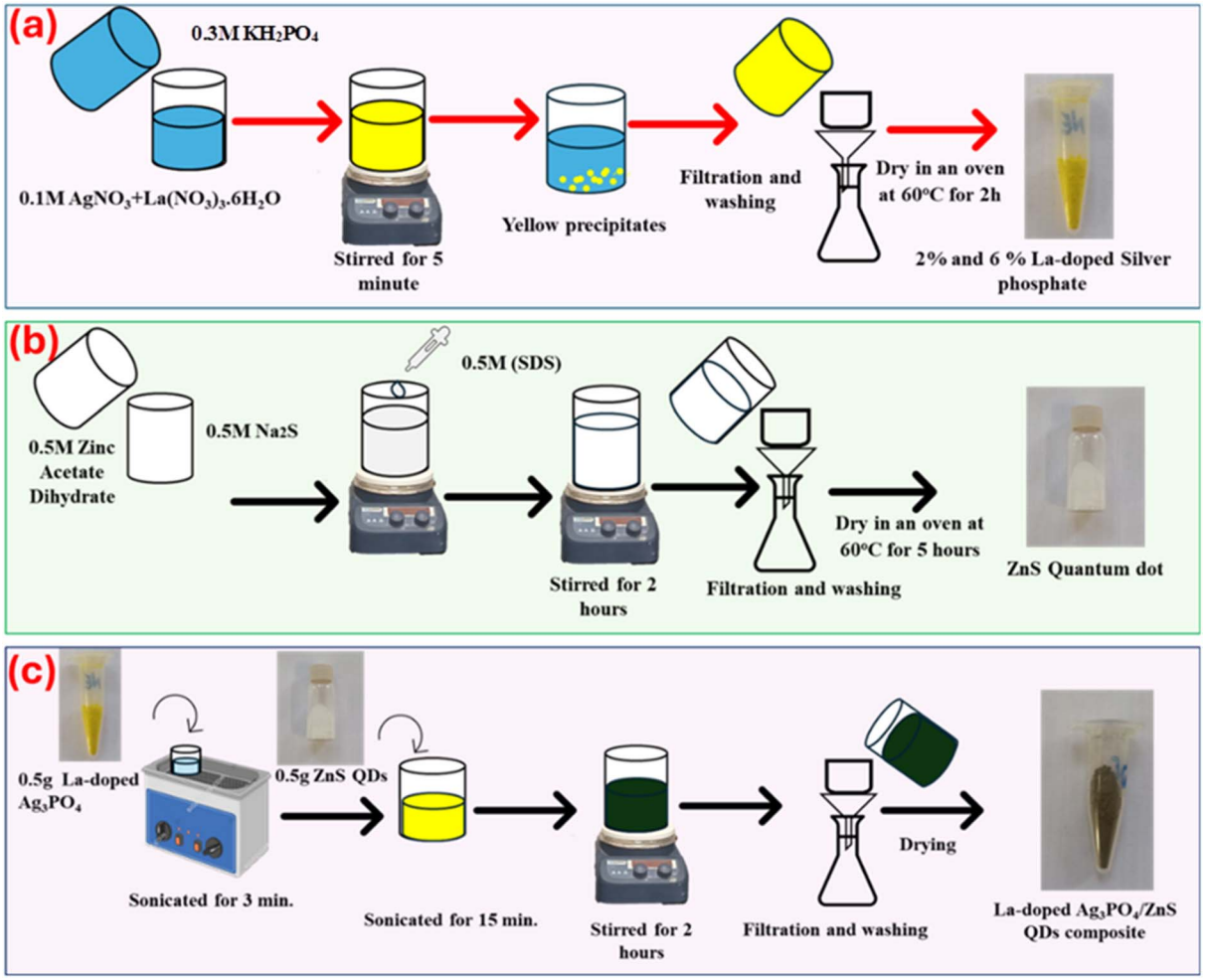

Fig. 1 Schematic of the synthesis routes to (a) doped and undoped Ag_3PO_4, (b) ZnS QDs, and (c) Ag_3PO_4/ZnS QD and La-doped Ag_3PO_4/ZnS QD composites.

Fig. S1(b). The equation used to determine the percentage of photocatalytic degradation is given below.[47]

$$\text{Percentage of degradation} = \frac{C_o - C_t}{C_o} \times 100 = \frac{A_o - A_t}{A_o} \times 100 \quad (1)$$

where A_o is the dye's initial absorbance, and A_t is its absorbance at time t.

3 Results and discussion

3.1 Characterization of the synthesized photocatalysts

Fig. 2(a) displays the XRD patterns of pure and doped silver phosphate (Ag_3PO_4).[26,32] In the XRD patterns of Ag_3PO_4 and La-doped Ag_3PO_4, the characteristic peaks observed at different 2θ values correspond to the (110), (200), (210), (211), (220), (310), (222), (320), (321), (400), and (411) planes, respectively.[26,32] All these peaks are well-matched with the JCPDS card no. 06-0505.[26,32] Compared to pure Ag_3PO_4, no change in the crystal structures and no impurity peaks are observed in the XRD patterns of 2% and 6% La-doped Ag_3PO_4, which indicates that the La(III) ions are successfully integrated and uniformly distributed in the host lattice. The XRD pattern of ZnS quantum dots (ZnS QDs) is also shown in Fig. 2(a).[48,49] In the XRD pattern of ZnS QDs, the major peaks observed at 2θ values of 29.20°, 48.53°, and 57.52° correspond to the (111), (220), and (311) planes, respectively. All these peaks are in accordance with JCPDS card no. 05-0566. The observed XRD pattern closely resembles the typical pattern of the cubic phase of the zinc blende structure.[49] The XRD patterns of the composites are displayed in Fig. 2(a). In the XRD patterns (Fig. 2(a)) of the composites, the diffraction peaks corresponding to Ag_3PO_4 and ZnS QDs are observed, confirming the coexistence of both phases in the composites. The crystal structure of Ag_3PO_4 is shown in Fig. 2(b).

The crystalline size of the synthesized materials was calculated using the Debye–Scherrer equation, as shown in eqn (2).[50]

$$D = \frac{0.94\lambda}{\beta \cos \theta} \quad (2)$$

The dislocation density (δ) was calculated using the following formula:[51]

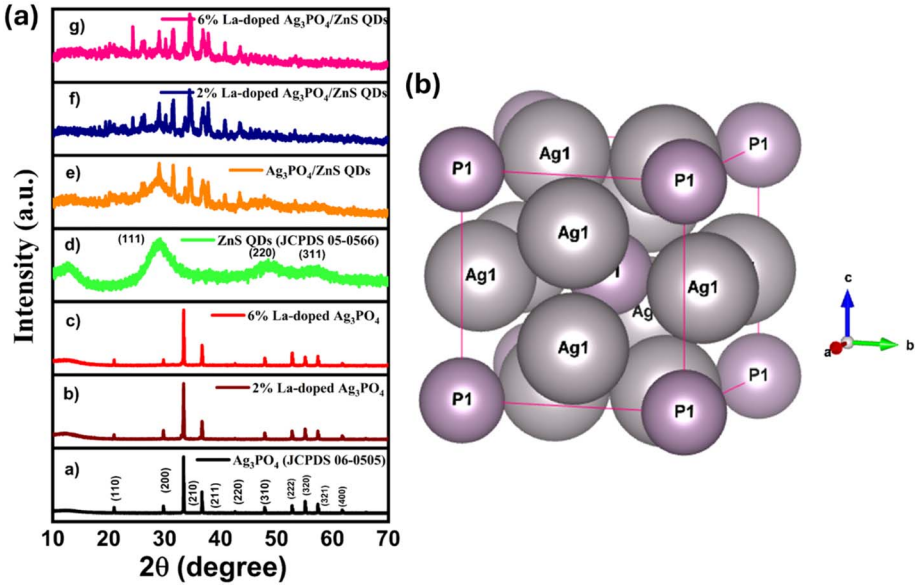

Fig. 2 (a) XRD patterns of the synthesized nanomaterials. (b) Crystal structure of silver phosphate.

$$\delta = \frac{1}{D^2} \tag{3}$$

The crystal microstain (ε) was calculated using the following formula:[52]

$$\varepsilon = \frac{\beta}{4 \tan \theta} \tag{4}$$

All calculated parameters are given in Table S1 in the SI. The average crystalline size of pure Ag_3PO_4 is found to be 158.13 nm. A clear reduction in the crystallite size is observed after La incorporation. The average crystallite sizes of 2% La-doped Ag_3PO_4 and 6% La-doped Ag_3PO_4 samples are 73.07 nm and 118 nm, respectively. This decrease can be attributed to the introduction of lattice strain and structural defects due to the addition of La, which restricts crystal growth, which is consistent with a previous report.[53] The calculated average crystallite size of the ZnS quantum dots is 2.26 nm, closely matching the previously reported value of 2.09 nm for ZnS quantum dots.[43,54] The Ag_3PO_4/ZnS composite further exhibits a reduced crystallite size of 10.33 nm. After the incorporation of La into this composite, the crystallite sizes are 37.80 and 21.54 nm for the 2% and 6% La-doped Ag_3PO_4, respectively.

FT-IR analysis was utilized to examine the functional groups of the synthesized materials. The FT-IR spectra of pure and La-doped Ag_3PO_4 are presented in Fig. 3(a). The main characteristic peaks are observed at 507, 550, 558, 670, 1007, and 2350 cm^{-1}, respectively. The peak observed at 507 cm^{-1} is due to the stretching vibrations of the Ag–O band, while the peak at 550 cm^{-1} corresponds to the O–P–O bending vibrations.[35] The stretching and bending vibrations of the P–O bond in the PO_4^{3-} group appear at 1007 and 558 cm^{-1}, respectively.[55–57] The peak at 2350 cm^{-1} is due to atmospheric carbon dioxide.[48] In the case of La-doped Ag_3PO_4, the main peak is observed at 610 cm^{-1}, corresponding to the La–O bond vibrations.[35]

In the FTIR spectrum of ZnS quantum dots (Fig. 3(a)), the main characteristic peaks appear at 651 cm^{-1} and 484 cm^{-1}, corresponding to the stretching vibrations of the Zn–S bond.[49,58] The absorption peaks at 1384,[59,60] 1419,[61] 1563[62] and 1620 cm^{-1} (ref. 61) correspond to the symmetric stretching vibrations of the $-COO^-$ bond. The broad peak observed at 3400 cm^{-1} is assigned to the stretching vibrations of the O–H bond, which arises from the adsorption of water molecules on the surface of ZnS.[63] The absorption peaks observed at 2852 cm^{-1} and 2921 cm^{-1} are attributed to the C–H stretching,[64] while the peaks at 1458 cm^{-1} and 1466 cm^{-1} correspond to the CH_3 bending vibrations.[65] The peak observed at 928 cm^{-1} is assigned to the S–C bond stretching vibrations.[66]

The Raman spectra of pure and doped Ag_3PO_4 are shown in Fig. 3(b). The Raman spectrum of pure Ag_3PO_4 displays distinct vibrational bands characteristic of the phosphate tetrahedron, which are closely related to those reported in a previous study.[67] The high-intensity band at 912 cm^{-1} is assigned to the stretching vibration of the terminal oxygen of the PO_4^{3-} groups. A weak band is observed at 555 cm^{-1}, which corresponds to the asymmetrical bending vibration of the P–O–P bond. In the case of La-doped Ag_3PO_4, no new band is identified in the range of 200–1800 cm^{-1}. However, the band at 912 cm^{-1} becomes progressively weaker and narrower with an increase in the concentration of La. Thus, the incorporation of La^{3+} alters only the intrinsic phosphate vibrations.

In the Raman spectrum of ZnS quantum dots (Fig. 3(b)), the characteristic bands appear at 270 cm^{-1} and 347 cm^{-1}, which correspond to the transverse optical (TO) and first-order longitudinal optical (1LO) phonon modes of cubic ZnS, respectively.[68–70] Additional bands appearing between ~997 and 1562 cm^{-1} are linked to multiphonon processes and SDS

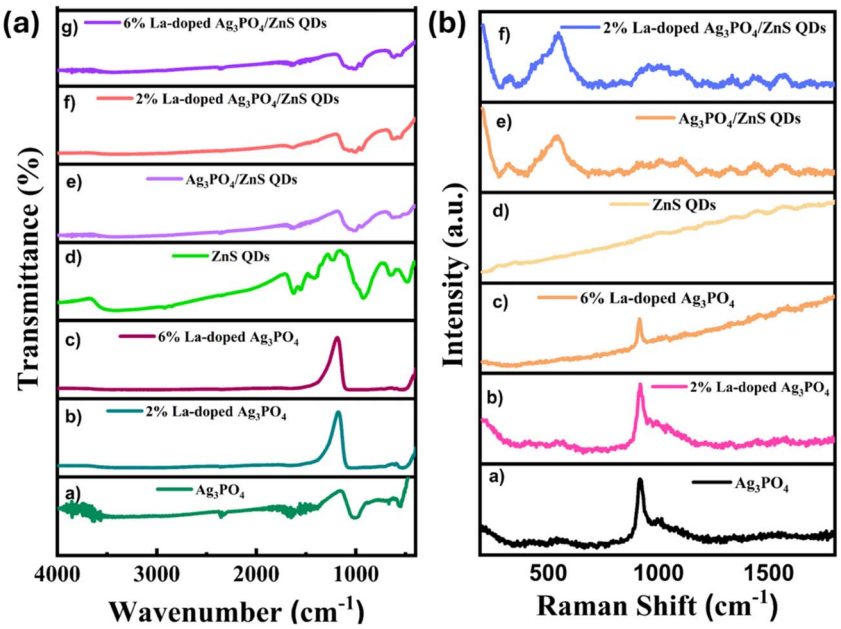

Fig. 3 (a) FTIR spectra of the synthesized nanomaterials. (b) Raman spectra of the synthesized nanomaterials.

vibrational modes.[71] These spectral characteristics not only confirm the structural crystallinity of ZnS QDs but also reveal the phonon confinement effects in nanocrystals. The Raman spectra of the composites display the vibrational modes of both components with slight band broadening, confirming that the two crystalline phases coexist in the composites.

The thermal stability of the synthesized photocatalysts was evaluated using thermogravimetric analysis (TGA), and the results are shown in Fig. 4(a). A slight weight loss is observed in the case of pure and doped Ag_3PO_4 up to 750 °C, demonstrating high thermal stability. The minor weight loss in these TGA curves is correlated with water loss. Similarly, the TGA curve of ZnS quantum dots, shown in Fig. 4(a), displays approximately 21% weight loss. The 7% weight loss at 150 °C is due to the removal of adsorbed water from the quantum dots' surface. However, the loss of sulfuric acid groups and degradation occur up to 400 °C. At 600 °C, the weight loss is due to the oxidation of ZnS to ZnO. Furthermore, in the case of Ag_3PO_4/ZnS quantum dot composites, three weight loss regions are observed up to 600 °C. The first weight loss at 150 °C corresponds to the loss of adsorbed water molecules, while the second one at 400 °C involves the evaporation of organic compounds. The final weight loss at 600 °C relates to the breakdown of the residual inorganic content, the oxidation of metal species, or internal structural modification.

The composite exhibits a 12% weight loss, indicating superior thermal stability compared to pure ZnS. In the doped composites, overall, 14% and 7.15% weight loss are observed for 6% La-doped Ag_3PO_4/ZnS and 2% La-doped Ag_3PO_4, respectively.

The optical characteristics of the synthesized catalysts were analysed by UV-visible diffuse reflectance spectroscopy (UV-DRS). The data were collected in terms of the reflectance (R) *versus* wavelength (λ), and the spectra are presented in Fig. 4(b). The band gap energies (E_g) were estimated using the Kubelka–Munk function, $F(R) = \frac{(1-R)^2}{2R}$,[72] and Tauc plots were created by plotting $(F(R)\cdot h\nu)^{1/2}$ against the photon energy ($h\nu$) (Fig. 4(c)). The band gap values were determined by extrapolating the linear portion of each Tauc plot to the energy axis. The calculated band gap energies are shown in Table 1.

Pure Ag_3PO_4 exhibits a band gap of 2.41 eV. Upon the addition of 2% and 6% La to the lattice, the band gap decreases slightly to 2.39 eV and 2.36 eV, respectively. The decrease in the band gap is possibly due to the creation of oxygen vacancies within the lattice upon La doping.[35] In contrast, ZnS QDs have a wider band gap of 3.60 eV and mainly absorb in the UV region. The 6% La-doped Ag_3PO_4/ZnS QD composite shows a markedly reduced band gap of 1.50 eV.

Photoluminescence (PL) spectroscopy was employed to identify defect sites and oxygen vacancies within the synthesized nanoparticles. As shown in Fig. 4(d), the results clearly indicate that all samples exhibit two distinct emission peaks. Pure Ag_3PO_4 exhibits two peaks at 436 and 463 nm.[73] 6% La-doped Ag_3PO_4 shows three peaks at 439, 468, and 507 nm. ZnS quantum dots (QDs) show two peaks at 439 and 467 nm. The 6% La-doped Ag_3PO_4/ZnS QD composite shows two peaks at 436 and 464 nm. It is observed that 6% La-doped Ag_3PO_4 shows an additional peak. The emission band observed within the 490–550 nm range is attributed to the radiative recombination of photogenerated charge carriers at surface-active oxygen vacancies.[74,75]

The surface area of the synthesized samples was investigated using BET analysis (Fig. 5(a)). The BET specific surface areas are determined to be 130.109, 89.934, 133.446, 116.537, and 141.120 $m^2\ g^{-1}$ for pure Ag_3PO_4, 2% La-Ag_3PO_4, 6% La-Ag_3PO_4,

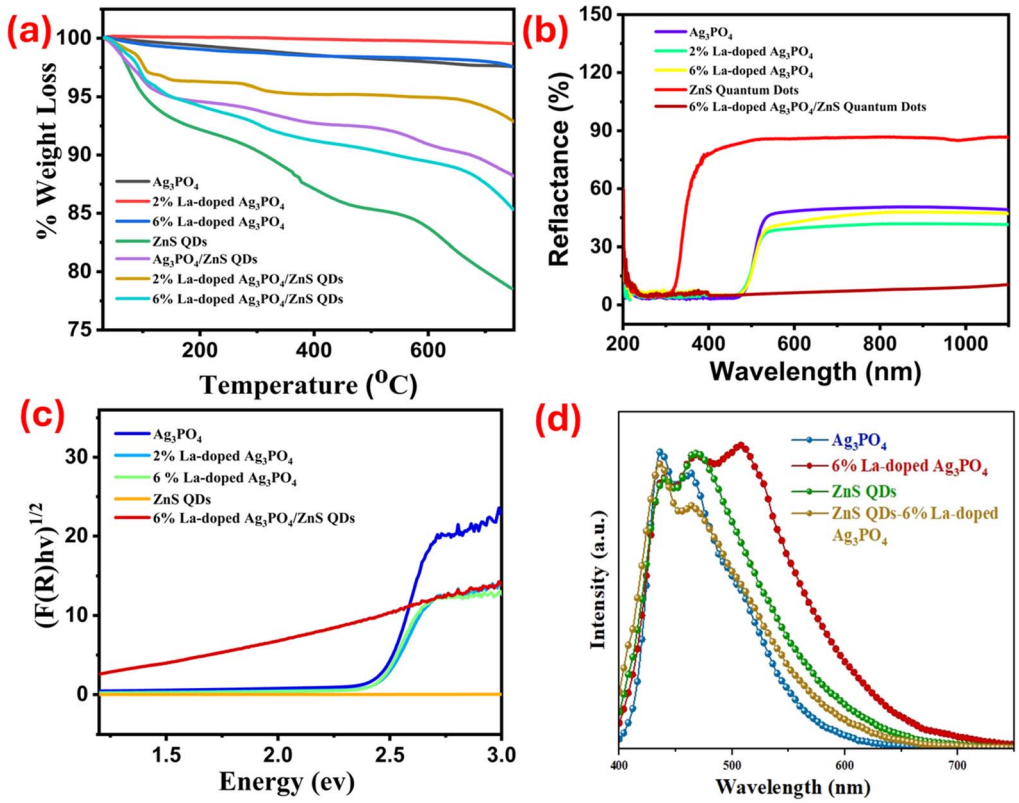

Fig. 4 (a) TGA analysis of the synthesized nanomaterials. (b) Relactance *vs.* wavelength spectra. (c) Tauc plots showing $(F(R)h\nu)^{\frac{1}{2}}$ *vs.* $h\nu$ for band gap estimation. (d) PL spectra of selected samples.

Table 1 Calculated band gap energies of different nanocatalysts

S. no.	Catalyst	Band gap (eV)
1	Pure Ag_3PO_4	2.41
2	2% La-doped Ag_3PO_4	2.39
3	6% La-doped Ag_3PO_4	2.36
4	ZnS quantum dots (QDs)	3.60
5	6% La-doped Ag_3PO_4/ZnS QD composite	1.50

ZnS QDs, and 6% La-Ag_3PO_4/ZnS QDs, respectively. Upon the incorporation of ZnS QDs into the 6% La-Ag_3PO_4 particles, the surface area of the 6% La-Ag_3PO_4 heterojunction composite increases from 133.446 to 141.120 $m^2\ g^{-1}$.

The pore size distribution of the samples was analysed by the BJH adsorption method (Fig. 5(b)). The pore radii of Ag_3PO_4, 2% La-Ag_3PO_4, 6% La-Ag_3PO_4, ZnS QDs, and 6% La-Ag_3PO_4/ZnS nanoparticles are 15.578, 15.564, 15.581, 15.610, and 14.761 Å, respectively. The pore sizes of Ag_3PO_4, 2% La-Ag_3PO_4, 6% La-Ag_3PO_4, ZnS QDs, and 6% La-Ag_3PO_4/ZnS nanoparticles are 3.116 nm, 3.113 nm, 3.116 nm, 3.122 nm, and 2.952 nm, respectively. This indicates a mesoporous structure according to the IUPAC classification (pores between 2 and 50 nm).[76]

Additionally, the pore volumes of Ag_3PO_4, 2% La-Ag_3PO_4, 6% La-Ag_3PO_4, ZnS QDs, and 6% La-Ag_3PO_4/ZnS are 0.036, 0.031, 0.038, 0.040, and 0.053 $cm^3\ g^{-1}$, respectively. This suggests that the BET surface area and pore size of the material are not the primary factors influencing its photocatalytic activity.[77] The comparison between different catalysts is presented in Fig. 5(c).

The surface morphology of the catalysts was studied using SEM images at various magnifications, as shown in Fig. 6(a–l). The pure Ag_3PO_4 particles have irregular spherical shapes with a porous, rough surface, and some are aggregated[78] (Fig. 6(a–d)). The SEM images of La-doped Ag_3PO_4 reveal that the morphology of silver phosphate changes from spherical to tetrapod, with a rough surface consisting of some pores (Fig. 6(e–h)). In the case of ZnS QDs, a regular morphology with slight agglomeration is observed, as shown in Fig. 6(i–l).[79]

The elemental composition of the materials was determined using energy-dispersive X-ray spectroscopy (EDS). The presence of Ag, P, and O elements in the EDS spectrum (Fig. 7(a)) of Ag_3PO_4 confirms the formation of Ag_3PO_4. In the case of 6% La-doped Ag_3PO_4, the EDS spectrum (Fig. 7(b)) displays the peaks of Ag, P, La, and O. The existence of the peaks of La in the EDS spectrum of 6% La-doped Ag_3PO_4 confirms that lanthanum (La) is successfully introduced into the lattice. The existence of carbon in the EDS spectra of pure and doped Ag_3PO_4 is probably due to the latex material of the SEM sample holder.[80] The presence of Zn and S peaks in the EDS spectrum (Fig. 7(c)) confirms the synthesis of the ZnS QDs. The presence of the small peaks of copper (Cu) and silicon (Si) in the EDS spectrum is due to the sample holder and EDS detector, respectively.

Fig. 8(a–f) presents the TEM micrographs of pure and 6% La-doped Ag_3O_4 at varying magnifications, revealing the

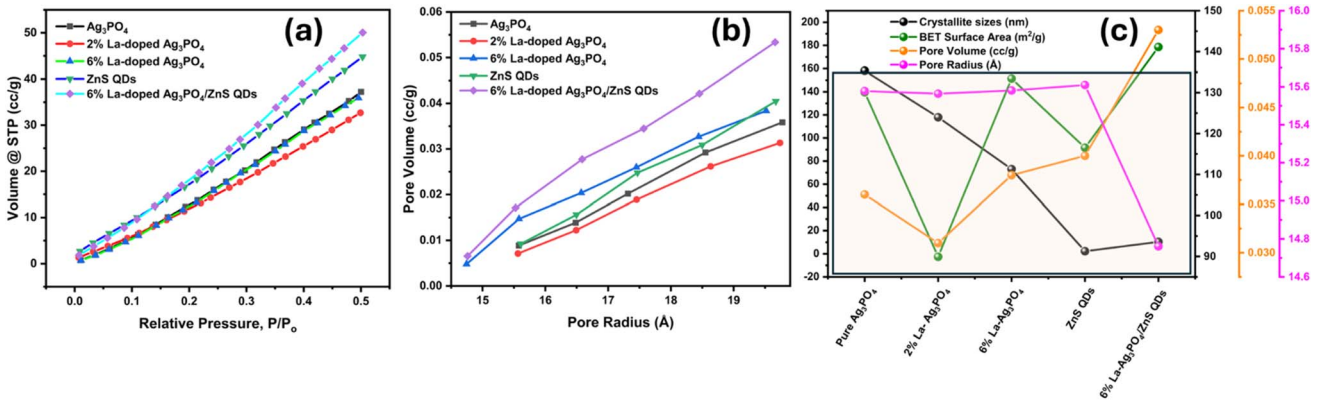

Fig. 5 (a) BET adsorption isotherms of the synthesized materials. (b) BJH adsorption-derived pore size distributions of the synthesized materials. (c) Comparison of the pore size, pore volume, and crystallite size of different catalysts.

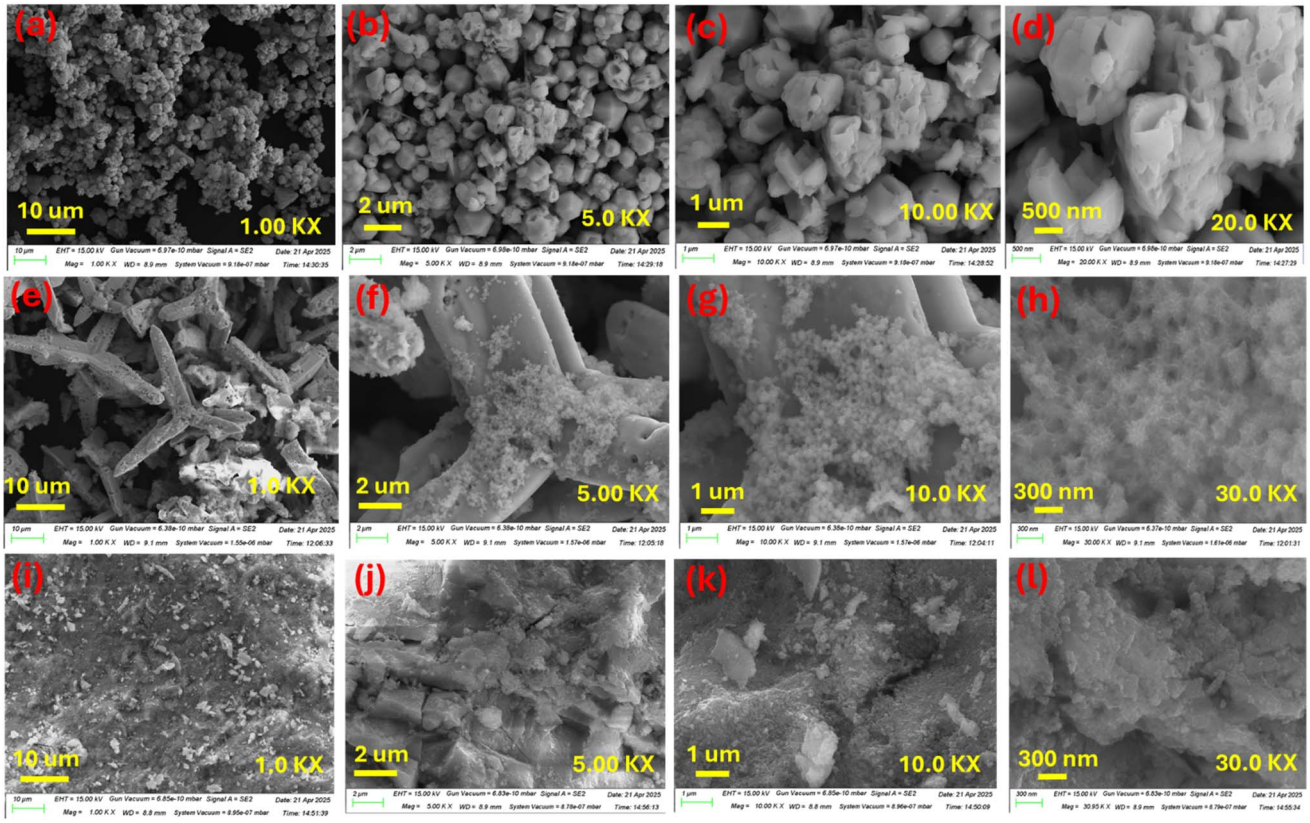

Fig. 6 SEM images of (a–d) Ag_3PO_4, (e–h) 6% La-doped Ag_3PO_4, and (i–l) ZnS quantum dots at different magnifications.

nanostructured morphology of the synthesized photocatalysts. The TEM micrograph of the nanoparticles shows that the synthesized nanoparticles are nearly spherical, tend to form soft agglomerates due to magnetic interactions, which range in size from 0.5 μm to less than 100 nm, and exhibit a smooth surface texture due to proper dispersion. The TEM images of ZnS are presented in Fig. 8(g–h).

The XPS survey spectra of La-Ag_3PO_4/ZnS nanocomposites reveal the presence of peaks corresponding to silver (Ag), oxygen (O), zinc (Zn), sulfur (S), phosphorus (P), lanthanum (La), and carbon (C), as illustrated in Fig. 9(a–f) and S2. The two characteristic peaks observed at 366.4 eV and 370.2 eV correspond to Ag $3d_{5/2}$ and Ag $3d_{3/2}$, respectively, indicating the presence of Ag^+ in Ag_3PO_4.[81] The O 1s peak at 530.2 eV corresponds to lattice oxygen in Ag_3PO_4.[82] As shown in Fig. 9(d), the Zn 2p spectrum displays two characteristic peaks at 1020.2 eV and 1044.5 eV, assigned to Zn $2p_{3/2}$ and Zn $2p_{1/2}$, respectively, confirming the presence of ZnS.[83] In the S 2p spectrum shown in Fig. 9(e), three distinct peaks are observed. The two peaks at binding energies of 162 and 163.1 eV are attributed to the S $2p_{3/2}$ and S $2p_{1/2}$ orbitals, respectively, confirming the presence of metal–sulfur bonds, such as those found in ZnS. The additional

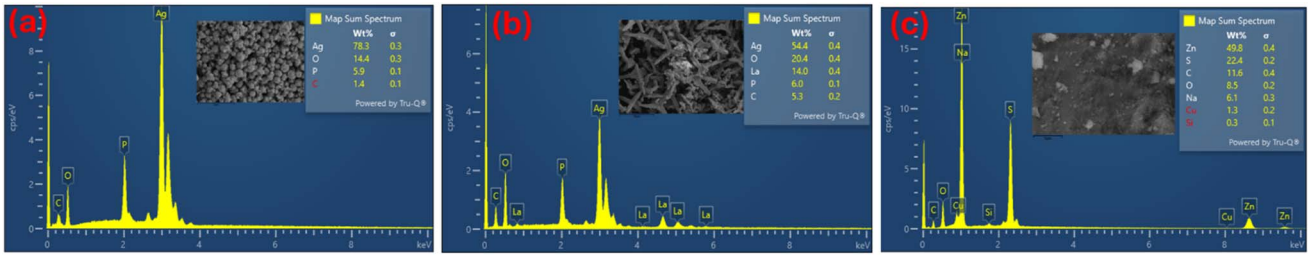

Fig. 7 EDS spectra of (a) Ag_3PO_4, (b) 6% La-doped Ag_3PO_4, and (c) ZnS QDs.

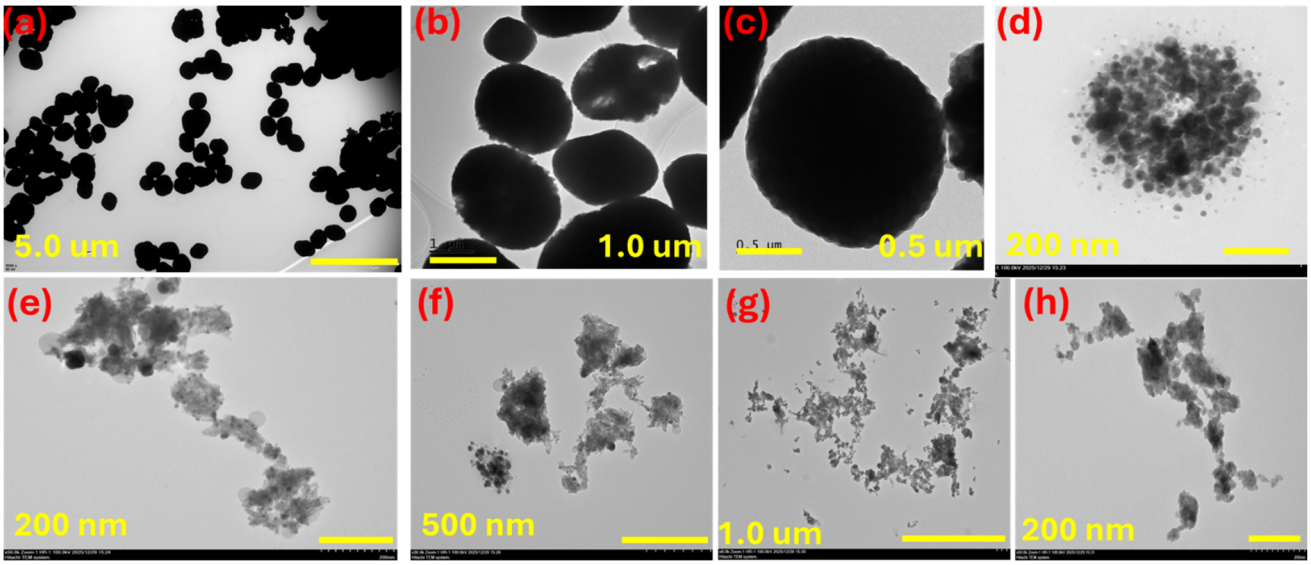

Fig. 8 TEM images of (a–c) pure Ag_3PO_4, (d–f) 6% La-Ag_3PO_4, and (g–h) ZnS QDs at different magnifications.

peak appearing at 169.1 eV is assigned to sulfur species in a higher oxidation state, which likely results from surface oxidation effects.[83]

The P 2p XPS spectrum shown in Fig. 9(b) exhibits a characteristic peak at a binding energy of 133.72 eV, which is attributed to phosphorus in the phosphate species.[84] The lanthanum 3d XPS spectrum is illustrated in Fig. 9(f). For lanthanum, the closed-shell La^{3+} ion shows La $3d_{5/2}$ and La $3d_{3/2}$ peaks. As shown in the spectrum, the La 3d peaks are deconvoluted into distinct subpeaks, with binding energies of 832.5 eV and 837.1 eV, corresponding to the La $3d_{5/2}$ and La $3d_{3/2}$ levels, respectively, confirming the presence of La in the trivalent oxidation state.[85] The deconvoluted C 1s XPS spectrum of Ag_3PO_4 nanoparticles, shown in Fig. S2(a), displays two distinct peaks at 284.2 eV and 286.9 eV. The C1 peak at 284.2 eV is assigned to sp^2-bonded carbon C–C, while the higher-binding-energy peak, C2, at 286.9 eV corresponds to C=O species. These results are consistent with the literature.[86] The complete XPS survey is shown in Fig. S2(b).

3.2 Application of the synthesized photocatalysts

3.2.1 Adsorption capacity of catalysts. The adsorption efficiency of all seven catalysts is illustrated in Fig. S3 of the SI. Results indicate that 6% La-doped Ag_3PO_4 exhibits the highest adsorption efficiency, at 64.93%, compared to other catalysts. Variations in adsorption efficiency can be linked to changes in the textural properties and surface functional groups of the catalysts.[87]

3.2.2 Photodegradation of azo dye (EBT). The photocatalytic activity of the prepared catalyst was tested for the photodegradation of Eriochrome Black T (EBT) under direct sunlight irradiation. The change in the color intensity of changes in 15 ppm standard EBT dye solutions under exposure to sunlight in the presence of different photocatalysts is shown in Fig. 10(a–f). Initially, the colour of the standard dye solutions is deep blue. As shown in Fig. 10(a–f), the colour of standard dye solutions changes from deep blue to colourless, indicating the successful breakdown of Eriochrome Black T in the presence of photocatalysts.

The results are presented in Fig. 11(a–f) and S4. The extent of dye degradation was examined by monitoring the change in the absorbance of the dye at regular intervals. The continuous decrease in absorbance with increasing irradiation time clearly indicates the effective photodegradation of EBT molecules. The photocatalytic activities of pure Ag_3PO_4, 2% La-doped Ag_3PO_4, 6% La-doped Ag_3PO_4, and ZnS quantum dots are 94.71%, 95.63%, 97.84% and 97.59%, respectively. Furthermore, the photocatalytic degradation efficiencies of the composite

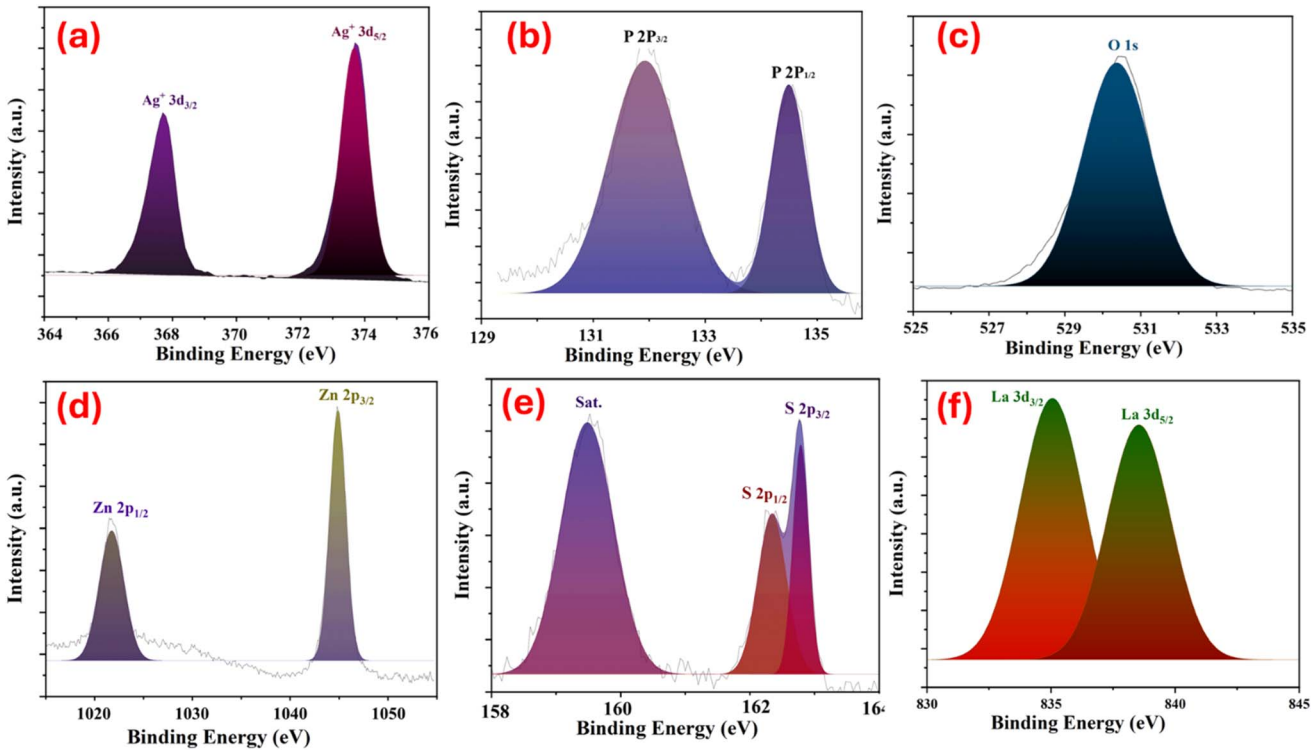

Fig. 9 XPS spectra of the La-doped Ag_3PO_4 decorated with ZnS quantum dots: (a) Ag 3d, (b) P 2p, (c) O 1s, (d) Zn 2p, (e) S 2p, and (f) La 3d.

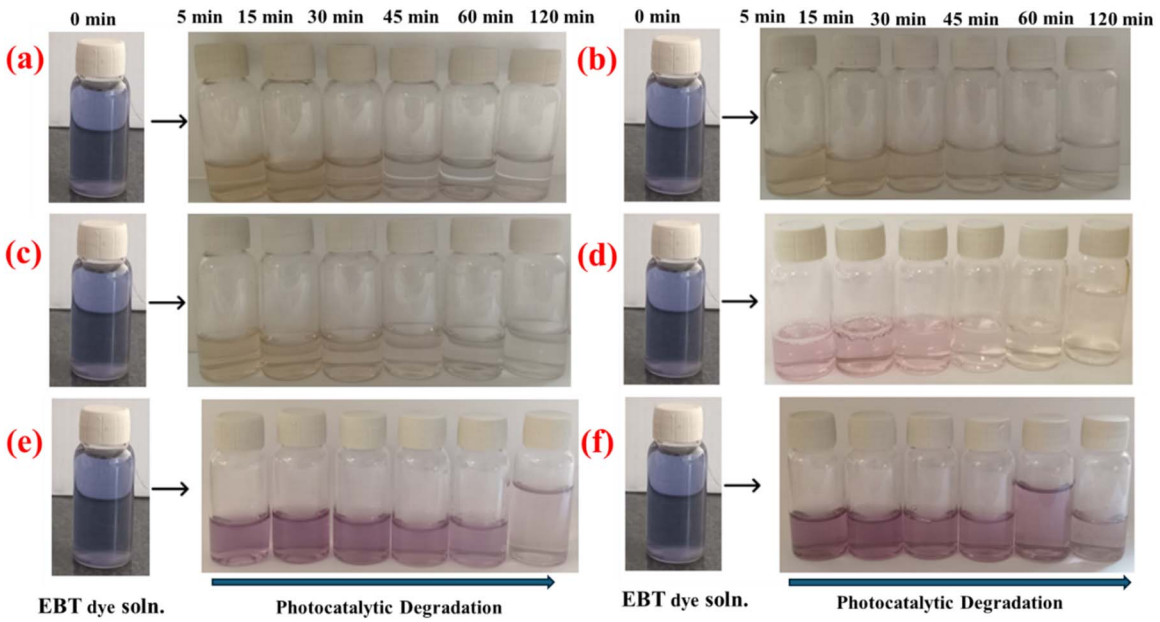

Fig. 10 Photographs showing colour intensity changes in 15 ppm standard dye solutions over time under exposure to sunlight using different photocatalysts: (a) pure Ag_3PO_4, (b) 2% La-doped Ag_3PO_4, (c) 6% La-doped Ag_3PO_4, (d) ZnS QDs, (e) Ag_3PO_4/ZnS quantum dots, and (f) 2% La-doped Ag_3PO_4/ZnS quantum dots.

materials, *i.e.*, Ag_3PO_4/ZnS QDs, 2% La-doped Ag_3PO_4/ZnS QDs, and 6% La-doped Ag_3PO_4/ZnS QDs, is 83.33%, 79.54%, and 84.88%, respectively.

La^{3+} doping improves photocatalytic activity primarily through lattice distortion and defect formation. As shown in Table S2, the crystallite size decreases with increasing La content, while the microstrain and dislocation density increase, indicating the introduction of structural defects. These defects increase the number of active sites and slightly reduce the band gap, enhancing light absorption and photocatalytic performance.

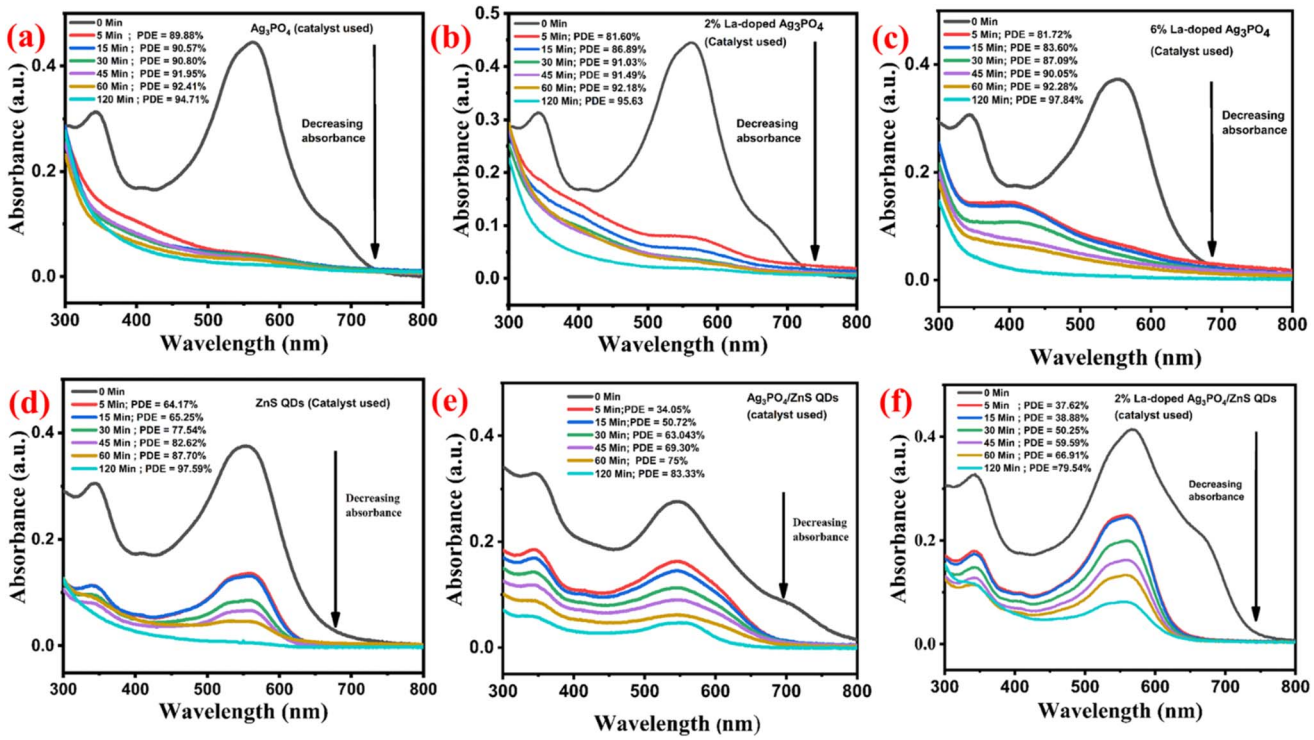

Fig. 11 Changes in the absorbance of a standard dye solution (15 ppm) with time for (a) pure Ag_3PO_4, (b) 2% La-doped Ag_3PO_4, (c) 6% La-doped Ag_3PO_4, (d) ZnS QDs, (e) Ag_3PO_4/ZnS quantum dots, and (f) 2% La-doped Ag_3PO_4/ZnS quantum dots. In each plot, the curves represent absorbance taken at different time intervals. The black, red, azure-blue, green, purple, amber orange and tiffany-blue lines correspond to 0, 5, 15, 30, 45, 60 and 120 min, respectively.

Although heterojunctions generally enhance photocatalytic activity, the lower degradation efficiency of the 6% La-Ag_3PO_4/ZnS composite than that of 6% La-Ag_3PO_4 can be explained by surface coverage effects. A similar behaviour has been reported for Ag_3PO_4/g-C_3N_4 composites, where the excessive loading of one component reduces photocatalytic activity due to the shielding of active sites.[88] In this work, the presence of ZnS may reduce the accessibility of Ag_3PO_4 active sites, leading to lower efficiency.

Although heterojunctions usually improve photocatalytic activity by reducing electron–hole recombination,[89] the 6% La-Ag_3PO_4/ZnS composite showed lower degradation efficiency than 6% La-Ag_3PO_4, likely because its low band gap (1.5 eV) can lead to faster charge recombination.

The slightly lower photocatalytic activity of the composite materials can be attributed to several factors. First, the combination of different components may have led to poor interfacial contact or inefficient charge transfer between the constituents, which hinders the separation and migration of photogenerated charge carriers. Second, there may have been an unfavourable band alignment between materials, preventing efficient electron–hole pair separation. Additionally, synthesis conditions or improper doping ratios might have resulted in surface defects, recombination centres, or agglomeration, all of which can negatively affect photocatalytic efficiency. These limitations collectively reduced the overall degradation efficiency of composites compared to individual photocatalysts.

3.3 Factors affecting the photocatalytic degradation of EBT

3.3.1 Effect of the amount of dye on photocatalytic efficiency. The concentration of dye plays an important role in the photocatalytic activity of a material. Three different concentrations (10, 15, and 20 ppm) of EBT were used to study their effect on the photocatalytic efficiency of seven different catalysts under direct sunlight. A fixed amount of the catalyst (0.1 g) was added to all samples in this experiment. The absorbance of all samples was measured at regular time intervals, and the results are presented in Fig. 12(a–f) and S5. The results indicated that the photodegradation efficiencies decreased with increasing concentration of EBT. The reason for this reduction in photodegradation is the decrease in the number of available surface active sites of photocatalysts to break down the dye molecules at a given time. Furthermore, the quantity of photons reaching the catalyst's surface decreases as the concentration of dye rises. This results in a low percentage of degradation because few OH radicals are produced.[44,90]

3.3.2 Effect of the amount of catalyst on photocatalytic efficiency. The effect of the amount of photocatalysts on the rate of dye degradation was studied using different concentrations of the catalyst, *i.e.*, 0.05 g, 0.1 g, and 0.15 g, in a fixed amount of dye (15 ppm) at room temperature. The results are illustrated in Fig. 13(a–f) and S6. According to the results, all catalysts showed increased photodegradation efficiencies with increasing amount of the catalyst from 0.05 to 0.15 g. An increase in the catalyst quantity results in more active sites on the

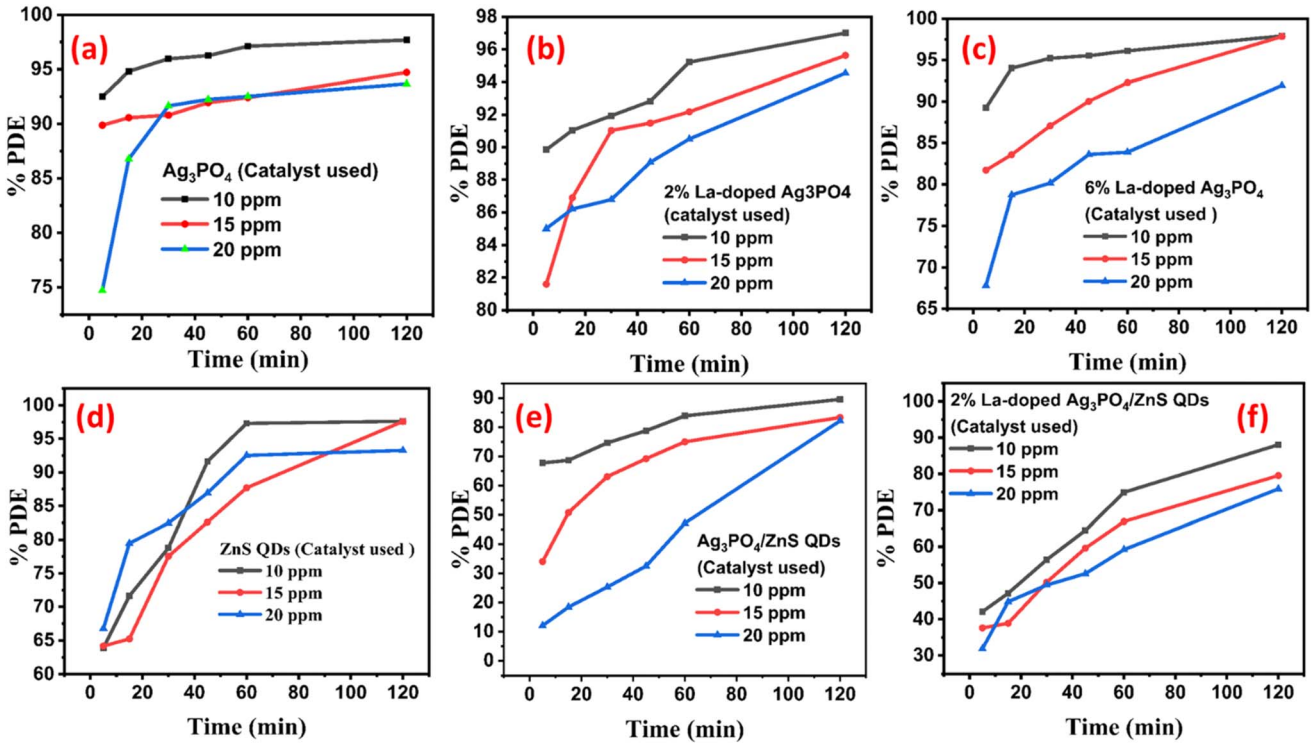

Fig. 12 (a–f) Effect of the initial dye concentration on the photocatalytic degradation of Eriochrome Black T using seven different catalysts. The black, red and blue curves correspond to 10, 15, and 20 ppm, respectively.

photocatalyst surface, which raises the quantity of $^{\cdot}OH$ radicals that can contribute to the dye solution's decolorization.[91]

3.3.3 Effect of pH on photocatalytic efficiency. pH is an important parameter in the photocatalytic degradation process because it influences the photocatalyst's surface charge, which influences dye degradation.[92,93] To study the effect of pH on the rate of EBT degradation, the experiment was conducted at three different pH levels, *i.e.*, 4, 6 (the natural pH of an EBT solution), and 10, using 6% La-doped Ag_3PO_4 and the 6% La-doped Ag_3PO_4/ZnS QD composite. Fig. S7(a and b) presents the influence of pH on the photodegradation efficiency of EBT using two different catalysts. At pH 6 (the original pH of the solution), the highest photodegradation efficiency of 97.84% was achieved using 6% La-doped Ag_3PO_4. The results indicated that the degradation efficiency increased as the pH changed from acidic (pH = 4) to near-neutral (pH = 6). Furthermore, the degradation efficiency decreased as the pH changed from neutral to basic conditions (pH = 10).

The impact of pH on the photocatalytic degradation performance of the catalyst is fundamentally explained by variations in the electric double layer at the solid-electrolyte interface. This variation in the electric double layer influences the adsorption–desorption process, generating electron–hole pairs on the photocatalyst surface. At low pH values (*e.g.*, pH = 4), the stronger adsorption of dye molecules reduces the number of active sites on the photocatalyst surface, thereby decreasing light absorption and photodegradation. Moreover, strong adsorption leads to the accumulation of multiple layers of dye molecules on the catalyst, hindering direct contact between dye molecules and the catalyst surface. Therefore, they do not participate in photodegradation.[94–96]

In case of 6% La-doped Ag_3PO_4/ZnS QD composite, the highest photodegradation efficiency of 88% was observed at pH 4. The higher photocatalytic activity is due to the effective electron–hole pair separation, higher dye adsorption capacity, and suitable band alignment between the 6% La-doped Ag_3PO_4 and ZnS QDs.

3.3.4 Effect of temperature on photocatalytic efficiency. Temperature plays a crucial role in the degradation of EBT. The effect of temperature on the degradation rate was studied by conducting experiments at 25 °C, 40 °C, and 50 °C using 6% La-doped Ag_3PO_4 and 6% La-doped Ag_3PO_4/ZnS QDs as photocatalysts. Fig. S7(c and d) illustrates the effect of temperature on the photodegradation efficiency of EBT. The rate of photodegradation gradually increased with increasing temperature. This increase in photocatalytic activity can be attributed to several factors. Firstly, raising the temperature enhances bubbling in the solution, which may increase the generation of free radicals. Furthermore, higher temperatures increase the oxidation of dye molecules at the catalyst-solution interface, further leading to improved photodegradation.[97]

Although degradation curves showed slight overlap for various factors (dye concentration, catalyst dose, pH, and temperature), it can be attributed to minor experimental variations in the sunlight intensity,[98] catalyst dispersion,[99] and light attenuation by dye molecules and other components in the solution.[98] Overall, the trends still clearly demonstrated how each factor affects EBT degradation.

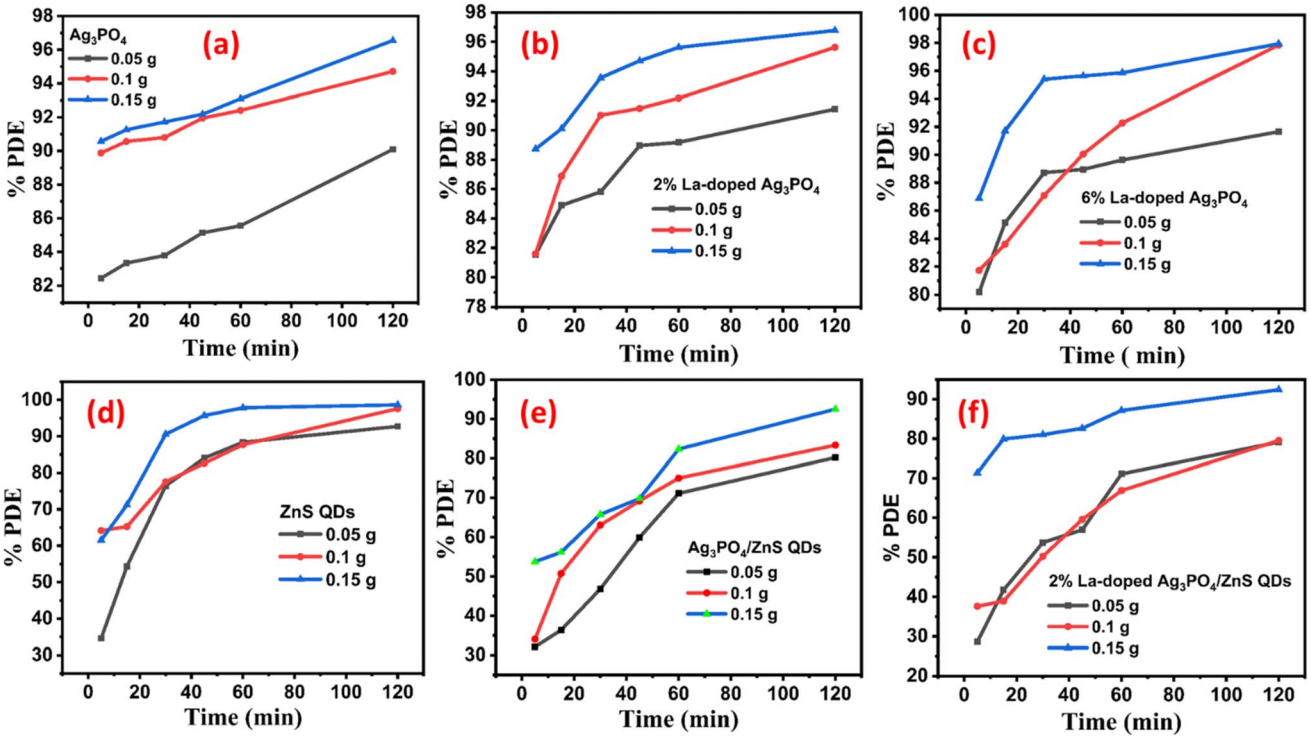

Fig. 13 (a–f) Effect of catalyst loading on the time-dependent photodegradation efficiency of EBT using seven different catalysts, each tested at three dosage levels. The black, red and blue curves correspond to 0.05, 0.1, and 0.15 g, respectively.

3.4 Kinetic study of the photodegradation process

The kinetic study of photodegradation was conducted using three kinetic models: zero-order, pseudo-first-order, and pseudo-second-order models.

In the case of pure Ag_3PO_4, 2–6% La-doped Ag_3PO_4, and the Ag_3PO_4/ZnS quantum dot composite, regression coefficient (R^2) values from the pseudo-second-order kinetic model were higher than the regression coefficient values from the zero-order kinetic model and pseudo-first-order kinetic model. The result showed that the degradation of EBT followed second-order kinetics. By contrast, in the case of ZnS quantum dots, the regression coefficient value ($R^2 = 0.94308$) from the pseudo-first-order kinetic model indicated that the degradation of EBT followed the first-order kinetics. In Fig. S8(a–c), the kinetic study of the photodegradation process of EBT for all catalysts is displayed.

3.5 Catalyst reusability

For practical applications, photocatalysts must exhibit not only high catalytic performance but also good stability and reusability. The reusability of the 6% La-doped Ag_3PO_4 photocatalyst was examined through repeated photocatalytic cycles. After each cycle, the catalyst was recovered, washed, and reused under the same reaction conditions. The results are shown in Fig. 14(a and b). The photocatalytic degradation efficiency of 6% La-silver phosphate is 97%, 91%, 85%, 77%, and 65% in cycles 1, 2, 3, 4, and 5, respectively. The decrease in degradation efficiency may be due to the loss of the photocatalyst during washing between cycles. The SEM images after 5 cycles are shown in Fig. 14(c and d).

Table S3 presents the recently reported efficiencies of various photocatalysts for the degradation of Eriochrome Black T (EBT). 6% La-doped Ag_3PO_4 and ZnS QDs exhibit superior performance under natural sunlight, achieving 97.84% and 97.59% degradation of EBT, respectively, within 120 minutes. Compared modified efficiency and operational simplicity.

3.6 Mechanism of photocatalytic degradation

Based on the UV-vis diffuse reflectance spectroscopy (DRS) results and photocatalytic degradation performance, a plausible photocatalytic mechanism is proposed. Under sunlight, Ag_3PO_4 (2.41 eV), 2% La-doped Ag_3PO_4 (2.39 eV), 6% La-doped Ag_3PO_4 (2.36 eV), ZnS QDs (3.6 eV), and 6% La-doped Ag_3PO_4/ZnS QDs (1.5 eV) generate electron–hole (e^-/h^+) pairs. The reduced band gap of the composite enhances sunlight absorption; however, an excessively low band gap may decrease the redox potential required for efficient photocatalytic reactions.[42] The photogenerated electrons are expected to react with dissolved oxygen to produce superoxide radicals ($^{\cdot}O_2^-$), while holes oxidize water to generate hydroxyl radicals ($^{\cdot}OH$), which are responsible for the degradation of the dye. These reactive species attack the dye adsorbed on the catalyst surface, breaking it down into simpler, less-toxic molecules.[37,100] Nevertheless, interfacial interactions in the composites may promote charge recombination, resulting in lower photocatalytic efficiency compared to the individual components. The chemical reactions involved in the degradation of EBT are presented in Fig. 15(a). The schematic diagram for EBT degradation *via* photocatalysts is shown in Fig. 15(b).

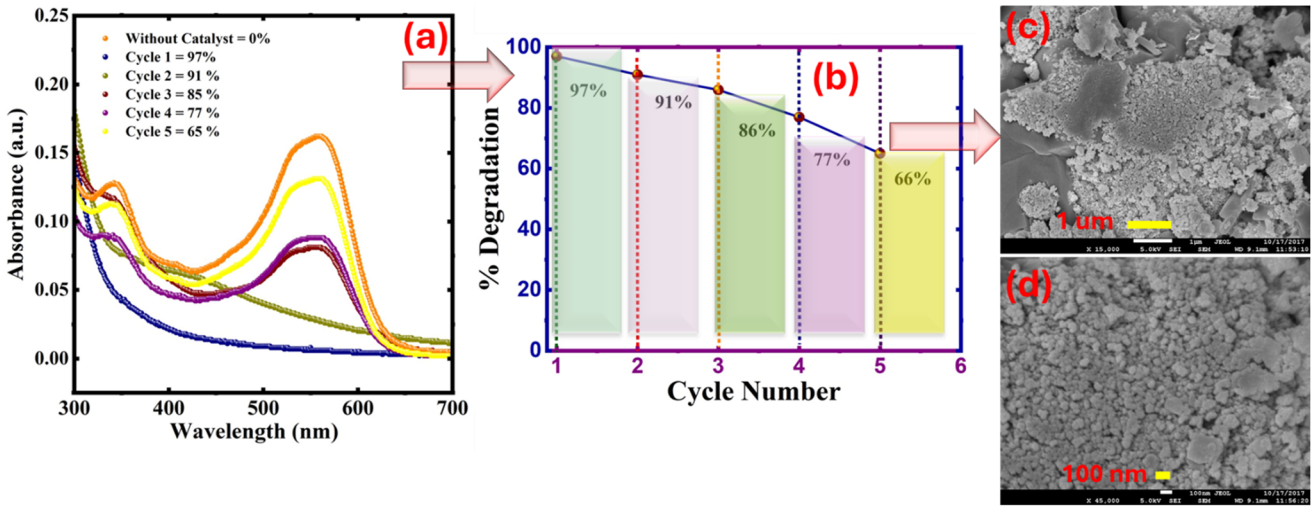

Fig. 14 (a and b) Catalyst reusability for up to 5 cycles using 6% La-Ag_3PO_4 in a 15 ppm dye solution. (c and d) SEM images after 5 cycles.

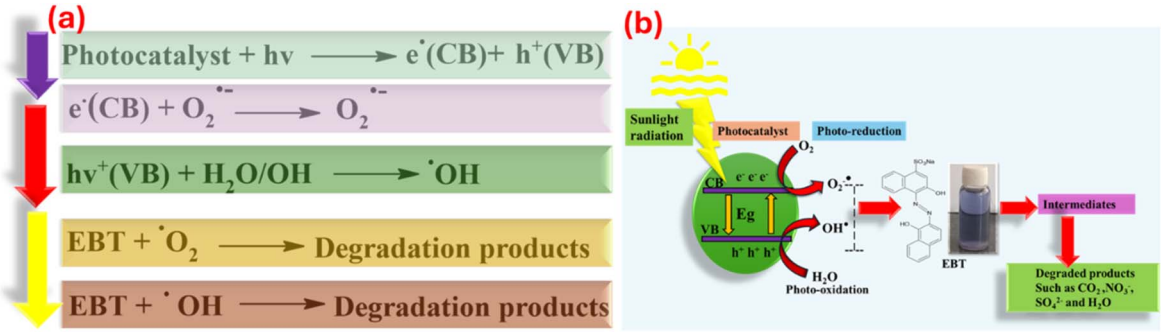

Fig. 15 (a) Photocatalytic degradation equations. (b) Schematic of EBT degradation using the proposed photocatalysts.

4 Conclusion

In summary, pure Ag_3PO_4, La-doped Ag_3PO_4 (2% and 6%), and ZnS quantum dots were successfully synthesized *via* a co-precipitation method, while the composites were synthesized through a hybrid mixing method. Different characterization techniques were used to analyse the structural, morphological, and optical properties of the synthesized materials. The XRD results confirmed the successful formation of crystalline Ag_3PO_4, La-doped Ag_3PO_4, ZnS quantum dots, and composites. The morphological study of the synthesized materials was performed using SEM micrographs. The elemental composition of the synthesized materials was confirmed by EDS analysis. TGA analysis indicated that all synthesized materials exhibited good thermal stability. UV-DRS results further verified that La incorporation into the Ag_3PO_4 lattice altered its band gap energy.

The photocatalytic capability of the synthesized materials was examined by observing the breakdown of Eriochrome Black T (EBT), an azo dye, under solar illumination. Notably, all synthesized individual materials showed higher degradation efficiency than the composites. This may be due to limitations such as inefficient charge separation and the limited availability of surface active sites on the composites. Additionally, particle clustering or weak interactions between the two components may have reduced the photocatalytic efficiency. Under the optimized reaction conditions, EBT photodegradation efficiencies of 97.84% and 84.88% were achieved using 6% La-doped Ag_3PO_4 and the 6% La-doped Ag_3PO_4/ZnS QD composite, respectively, at pH 6, with an initial dye concentration of 15 ppm, a photocatalyst dosage of 0.1 g, and an irradiation time of 120 min. Among the tested materials, 6% La-doped Ag_3PO_4 showed the highest photocatalytic performance, which can be attributed to enhanced charge carrier utilization and favourable electronic interactions resulting from lanthanum doping. These results indicate that La-modified Ag_3PO_4-based photocatalysts are promising and sustainable materials for the effective treatment of dye-contaminated wastewater, offering significant potential for environmental remediation applications.

Author contributions

Shabana Bibi: experimental work, writing original draft; Dr Amna Bashir, Dr Noshabah Tabassum: supervision, data analysis, writing, proofreading. The rest of the authors helped in the characterization of materials.

Conflicts of interest

There is no conflict of interest.

Data availability

Data would be made available on request.

Supplementary information (SI) is available. See DOI: https://doi.org/10.1039/d6ra00544f.

Acknowledgements

This research work was supported by the Ministry of Higher Education (MOHE) under the 2023 Translational Research Program for the Energy Sustainability Focus Area (Project ID: MMUE/240001), the 2024 ASEAN IVO (Project ID: 2024-02), and Multimedia University, Malaysia.

References

1 F. Arias Arias, M. Guevara, T. Tene, P. Angamarca, R. Molina, A. Valarezo, O. Salguero, C. Vacacela Gomez, M. Arias and L. S. Caputi, The adsorption of methylene blue on eco-friendly reduced graphene oxide, *Nanomaterials*, 2020, **10**(4), 681.

2 S. Jayapandi, P. Backialakshmi, P. Soundarrajan, M. Senthil Pandian, P. Ramasamy, S. Suresh Kumar and C. Gopinathan, Construction of p–n junction type Ag2O/SnO2 heterostructure photocatalyst for enhanced organic dye degradation under direct sunlight irradiation: Experimental and theoretical investigations, *J. Mater. Res.*, 2023, **38**(3), 753–766.

3 M. Khatun, P. Mitra and S. Mukherjee, Effect of band gap and particle size on photocatalytic degradation of NiSnO3 nanopowder for some conventional organic dyes, *Hybrid Adv.*, 2023, **4**, 100079.

4 T. Naseem and T. Durrani, The role of some important metal oxide nanoparticles for wastewater and antibacterial applications: A review, *Environ. Chem. Ecotoxicol.*, 2021, **3**, 59–75.

5 M. Al-Ghouti, M. Khraisheh, S. Allen and M. Ahmad, The removal of dyes from textile wastewater: a study of the physical characteristics and adsorption mechanisms of diatomaceous earth, *J. Environ. Manag.*, 2003, **69**(3), 229–238.

6 A. Alinsafi, M. Khemis, M.-N. Pons, J.-P. Leclerc, A. Yaacoubi, A. Benhammou and A. Nejmeddine, Electro-coagulation of reactive textile dyes and textile wastewater, *Chem. Eng. Process. Process Intensif.*, 2005, **44**(4), 461–470.

7 A. Bashir, F. Bashir, Z. Mehmood, M. S. Satti and Z. Akhter, Synthesis, characterisation and investigation of enhanced photocatalytic activity of Sm+ 3, Ni+ 2 co-doped TiO2 nanoparticles on the degradation of azo dyes in visible region, *Int. J. Nanoparticles*, 2019, **11**(1), 37–61.

8 R. Rashidi, Y. Omidi Khaniabadi and M. Ghaderpoori, Adsorption of Eriochrome black-T from aqueous environment by raw Montmorillonite, *Int. J. Environ. Anal. Chem.*, 2023, **103**(11), 2601–2615.

9 N. Barka, M. Abdennouri and M. E. Makhfouk, Removal of Methylene Blue and Eriochrome Black T from aqueous solutions by biosorption on Scolymus hispanicus L.: Kinetics, equilibrium and thermodynamics, *J. Taiwan Inst. Chem. Eng.*, 2011, **42**(2), 320–326.

10 M. Alamzeb, M. Tullah, S. Ali, Ihsanullah, B. Khan, W. N. Setzer, N. Al-Zaqri and M. N. M. Ibrahim, Kinetic, thermodynamic and adsorption isotherm studies of detoxification of Eriochrome Black T dye from wastewater by native and washed garlic peel, *Water*, 2022, **14**(22), 3713.

11 M. T. Yagub, T. K. Sen, S. Afroze and H. M. Ang, Dye and its removal from aqueous solution by adsorption: a review, *Adv. Colloid Interface Sci.*, 2014, **209**, 172–184.

12 F. Moeinpour, A. Alimoradi and M. Kazemi, Efficient removal of Eriochrome black-T from aqueous solution using NiFe2O4 magnetic nanoparticles, *J. Environ. Health Sci. Eng.*, 2014, **12**(1), 112.

13 A. V. Padalkar and R. Kumar, Common effluent treatment plant (CETP): Reliability analysis and performance evaluation, *Water Sci. Eng.*, 2018, **11**(3), 205–213.

14 J. Rathore, Studies on pollution load induced by dyeing and printing units in River Bandi at Pali, Rajasthan, India, *Int. J. Environ. Sci.*, 2012, **3**(1), 735–742.

15 S. Garcia-Segura, J. D. Ocon and M. N. Chong, Electrochemical oxidation remediation of real wastewater effluents—A review, *Process Saf. Environ. Prot.*, 2018, **113**, 48–67.

16 E. S. Priya and P. S. Selvan, Water hyacinth (Eichhornia crassipes)–An efficient and economic adsorbent for textile effluent treatment–A review, *Arab. J. Chem.*, 2017, **10**, S3548–S3558.

17 K. K. Wilson, *Assessment of the impact of effluents discharge from Murang'a town and its environs on the water quality of river Mathioya, Murang'a County, Kenya, COPAS, JKUAT*, 2017, pp. 1–84.

18 A. Srivastava, N. Verma, A. Mistri, B. Ranjan, A. K. Nigam, U. Kumari, S. Mittal and A. K. Mittal, Alterations in the skin of Labeo rohita exposed to an azo dye, Eriochrome black T: a histopathological and enzyme biochemical investigation, *Environ. Sci. Pollut. Res.*, 2017, **24**(9), 8671–8681.

19 M. Al Kausor and D. Chakrabortty, Graphene oxide based semiconductor photocatalysts for degradation of organic dye in waste water: A review on fabrication, performance enhancement and challenges, *Inorg. Chem. Commun.*, 2021, **129**, 108630.

20 C. M. Simonescu, A. Tătăruş, D. C. Culiţă, N. Stănică, I. A. Ionescu, B. Butoi and A.-M. Banici, Comparative study of CoFe2O4 nanoparticles and CoFe2O4-chitosan composite for Congo red and methyl orange removal by adsorption, *Nanomaterials*, 2021, **11**(3), 711.

21 F. Harrelkas, A. Paulo, M. Alves, L. El Khadir, O. Zahraa, M.-N. Pons and F. Van Der Zee, Photocatalytic and combined anaerobic–photocatalytic treatment of textile dyes, *Chemosphere*, 2008, **72**(11), 1816–1822.

22 Y. Bi, H. Hu, S. Ouyang, G. Lu, J. Cao and J. Ye, Photocatalytic and photoelectric properties of cubic Ag 3 PO 4 sub-microcrystals with sharp corners and edges, *Chem. Commun.*, 2012, **48**(31), 3748–3750.

23 L. Dong, P. Wang, S. Wang, P. Lei and Y. Wang, A simple way for Ag3PO4 tetrahedron and tetrapod microcrystals with high visible-light-responsive activity, *Mater. Lett.*, 2014, **134**, 158–161.

24 J. Cruz-Filho, T. Costa, M. Lima, L. Silva, R. Santos, L. Cavalcante, E. Longo and G. Luz Jr, Effect of different synthesis methods on the morphology, optical behavior, and superior photocatalytic performances of Ag3PO4 sub-microcrystals using white-light-emitting diodes, *J. Photochem. Photobiol., A*, 2019, **377**, 14–25.

25 A. Khan, M. Qamar and M. Muneer, Synthesis of highly active visible-light-driven colloidal silver orthophosphate, *Chem. Phys. Lett.*, 2012, **519**, 54–58.

26 E. Ghazalian, N. Ghasemi and A. Amani-Ghadim, Enhanced visible light photocatalytic performance of Ag3PO4 through doping by different trivalent Lanthanide cations, *Mater. Res. Bull.*, 2017, **88**, 23–32.

27 M. S. Hussien and I. Yahia, Fabrication progress of selective and durable Ni2+-doped Ag3PO4 for visible-light degradation of various textile dyes, *J. Photochem. Photobiol., A*, 2019, **368**, 210–218.

28 S. Zhang, S. Zhang and L. Song, Super-high activity of Bi3+ doped Ag3PO4 and enhanced photocatalytic mechanism, *Appl. Catal. B Environ.*, 2014, **152**, 129–139.

29 W. Cao, Z. Gui, L. Chen, X. Zhu and Z. Qi, Facile synthesis of sulfate-doped Ag3PO4 with enhanced visible light photocatalytic activity, *Appl. Catal. B Environ.*, 2017, **200**, 681–689.

30 J. Luo, Y. Luo, Q. Li, J. Yao, G. Duan and X. Liu, Synthesis of doughnut-like carbonate-doped Ag3PO4 with enhanced visible light photocatalytic activity, *Colloids Surf., A*, 2017, **535**, 89–95.

31 S. Li, S. Shi, G. Huang, Y. Xiong and S. Liu, Synergetic tuning charge dynamics and potentials of Ag3PO4 photocatalysts with boosting activity and stability by facile in-situ fluorination, *Appl. Surf. Sci.*, 2018, **455**, 1137–1149.

32 Y. P. Xie and G. S. Wang, Visible light responsive porous Lanthanum-doped Ag3PO4 photocatalyst with high photocatalytic water oxidation activity, *J. Colloid Interface Sci.*, 2014, **430**, 1–5.

33 S. Anandan, A. Vinu, K. S. Lovely, N. Gokulakrishnan, P. Srinivasu, T. Mori, V. Murugesan, V. Sivamurugan and K. Ariga, Photocatalytic activity of La-doped ZnO for the degradation of monocrotophos in aqueous suspension, *J. Mol. Catal. A: Chem.*, 2007, **266**(1–2), 149–157.

34 H. Kato, K. Asakura and A. Kudo, Highly efficient water splitting into H2 and O2 over lanthanum-doped NaTaO3 photocatalysts with high crystallinity and surface nanostructure, *J. Am. Chem. Soc.*, 2003, **125**(10), 3082–3089.

35 A. Amirulsyafiee, M. M. Khan, M. Y. Khan, A. Khan and M. H. Harunsani, Visible light active La-doped Ag3PO4 for photocatalytic degradation of dyes and reduction of Cr (VI), *Solid State Sci.*, 2022, **131**, 106950.

36 B. Wang, Y. Liu, H. Hao, Y. Zhao, Z. He, W. Song, E. Liu, Z. Li and Z. Miao, Alteration of internal electron migration pathways in La-doped Ag 3 PO 4 for improved photocatalytic stability, *Mater. Chem. Front.*, 2025, **9**(7), 1189–1204.

37 D. Chen, F. Huang, G. Ren, D. Li, M. Zheng, Y. Wang and Z. Lin, ZnS nano-architectures: photocatalysis, deactivation and regeneration, *Nanoscale*, 2010, **2**(10), 2062–2064.

38 C. Venkata Reddy, N. Bandaru, J. Shim and S. P. Vattikuti, Synthesis of CdO/ZnS heterojunction for photodegradation of organic dye molecules, *Appl. Phys. A*, 2017, **123**(6), 396.

39 K. Sharma, P. Raizada, V. Hasija, P. Singh, A. Bajpai, V.-H. Nguyen, S. Rangabhashiyam, P. Kumar, A. K. Nadda and S. Y. Kim, ZnS-based quantum dots as photocatalysts for water purification, *J. Water Proc. Eng.*, 2021, **43**, 102217.

40 Y. Zhao, X. Wu, H. Wang, M. Ma, J. Tian and X. Wang, Phosphorus regulates coordination number and electronegativity of cobalt atomic sites triggering efficient photocatalytic water splitting, *Nano Lett.*, 2024, **24**(50), 16175–16183.

41 C. Xing, J. Ren, L. Fan, J. Zhang, M. Ma, S. Wu, Z. Liu and J. Tian, π-d conjugated copper chloranilate with distorted Cu-O4 site for efficient electrocatalytic ammonia production, *Adv. Funct. Mater.*, 2024, **34**(49), 2409064.

42 S. M. Yahaya, N. Abdu, I. A. Aliyu and B. Mukhtar, Revolutionizing nitrogen fixation: communicating the potentials of nanostructured photocatalysts for sustainable ammonia/nitrate synthesis, *Circ. Agric. Syst.*, 2024, **4**(1), 1–13.

43 S. Kaur, S. Sharma, A. Umar, S. Singh, S. Mehta and S. K. Kansal, Solar light driven enhanced photocatalytic degradation of brilliant green dye based on ZnS quantum dots, *Superlattices Microstruct.*, 2017, **103**, 365–375.

44 A. Bashir, F. Bashir, M. Sultan, M. Mubeen, A. Iqbal and Z. Akhter, Influence of nickel and lanthanum ions co-doping on photocatalytic properties of TiO2 for effective degradation of reactive yellow 145 in the visible region, *J. Sol-Gel Sci. Technol.*, 2020, **93**(2), 438–451.

45 R. A. Shathy, S. A. Fahim, M. Sarker, M. S. Quddus, M. Moniruzzaman, S. M. Masum and M. A. I. Molla, Natural sunlight driven photocatalytic removal of toxic textile dyes in water using B-doped ZnO/TiO2 nanocomposites, *Catalysts*, 2022, **12**(3), 308.

46 K. Bano, S. K. Mittal, P. P. Singh and S. Kaushal, Sunlight driven photocatalytic degradation of organic pollutants using a MnV 2 O 6/BiVO 4 heterojunction: Mechanistic perception and degradation pathways, *Nanoscale Adv.*, 2021, **3**(22), 6446–6458.

47 J. Goyal, S. Sharma and S. Basu, Solar light-induced photocatalytic response of BiOCl/PANI composite towards the degradation of tetracycline, *Catalysts*, 2023, **13**(5), 795.

48 H. Yu and M. Obrovac, Quantitative determination of carbon dioxide content in organic electrolytes by infrared spectroscopy, *J. Electrochem. Soc.*, 2019, **166**(12), A2467.

49 A. B. Alwany, G. Youssef, O. Samir, M. A. Algradee, N. A. A. Yahya, M. A. Swillam, S. Humaidi and R. Abd-Shukor, Annealing temperature effects on the size and band gap of ZnS quantum dots fabricated by co-precipitation technique without capping agent, *Sci. Rep.*, 2023, **13**(1), 10314.
50 A. Patterson, The Scherrer formula for X-ray particle size determination, *Phys. Rev.*, 1939, **56**(10), 978.
51 M. Srivathsa and B. V. Rajendra, Effect of lanthanum doping on the structural, morphological, and optical properties of spray-coated ZnO thin films, *Eng. Proc.*, 2023, **59**(1), 32.
52 S.-Y. Ting, P.-J. Chen, H.-C. Wang, C.-H. Liao, W.-M. Chang, Y.-P. Hsieh and C. Yang, Crystallinity improvement of ZnO thin film on different buffer layers grown by MBE, *J. Nanomater.*, 2012, **2012**(1), 929278.
53 A. A. Khan, A. T. Partho, M. H. Arnab, M. A. Khyam, N. Kumar and M. Tahir, Recent advances in Lanthanum-based photocatalysts with engineering aspects for photocatalytic hydrogen production: A critical review, *Mater. Sci. Semicond. Process.*, 2024, **184**, 108809.
54 L. Saravanan, S. Diwakar, R. Mohankumar, A. Pandurangan and R. Jayavel, Synthesis, structural and optical properties of PVP encapsulated CdS nanoparticles, *Nanomater. Nanotechnol.*, 2011, **1**, 17.
55 Y. Yue, L. Han, B. Ding, Y. Yang, X. Yue, S. Wang, Q. Song and C. Du, Straw-derived activated carbon decorated with Ag3PO4 for organic pollutant removal by a circular degradation mechanism: adsorption and photocatalysis, *ACS Omega*, 2024, **9**(22), 23584–23596.
56 Y. Wang, M. Ding, Z. Li and M. Li, Visible light photocatalytic degradation of dyes by Ag3PO4/g-C3N4/CQDs composite, *Surf. Interfaces*, 2024, **44**, 103585.
57 Y. Wang, J. Niu, X. Gao and Y. Zhang, Synergetic tuning of photocatalytic activity and photostability of Ag3PO4 via yttrium doping, carbon quantum dots and BiVO4 for atenolol degradation, *Appl. Surf. Sci.*, 2020, **533**, 147458.
58 A. Dhupar, S. Kumar, H. S. Tuli, A. K. Sharma, V. Sharma and J. K. Sharma, In-doped ZnS nanoparticles: structural, morphological, optical and antibacterial properties, *Appl. Phys. A*, 2021, **127**(4), 263.
59 A. Sudha, I. Manimehan and P. Sakthivel, Structural, morphological, electrochemical and optical properties ZnS quantum dots: Influence of La3+ ions, *Results Opt.*, 2024, **16**, 100727.
60 P. Sakthivel, A. Krishnamoorthy and I. Devadoss, Influence of Fe3+ ions on the crystallographic, optical and electrochemical performance of ZnS quantum dots, *Indian J. Phys.*, 2024, **98**(3), 937–946.
61 A. Jain, S. Panwar, T. Kang, H. Jeon, S. Kumar and R. Choubey, Effect of zinc oxide concentration in fluorescent ZnS: Mn/ZnO core–shell nanostructures, *J. Mater. Sci.: Mater. Electron.*, 2014, **25**(4), 1716–1723.
62 A. B. Alwany, G. Youssef, E. E. Saleh, M. A. Algradee, A. Alnakhlani and B. Hassan, Effect of lead doping on the structural, optical, and radiation shielding parameters of chemically synthesized ZnS nanoparticles, *J. Mater. Sci.: Mater. Electron.*, 2023, **34**(3), 233.
63 P. Sakthivel and S. Muthukumaran, Crystallographic, structural and band gap tailoring of Zn0. 98Mn0. 02S quantum dots co-doped with Cu by co-precipitation method, *J. Inorg. Organomet. Polym. Mater.*, 2016, **26**(3), 563–571.
64 T. Watanabe, C. Wada, Y. Iso, T. Isobe and H. Sasaki, Preparation of photostable fluorescent InP/ZnS quantum dots embedded in TMAS-derived silica, *ECS J. Solid State Sci. Technol.*, 2017, **6**(7), R75.
65 H. Qu, L. Cao, G. Su, W. Liu, R. Gao, C. Xia and J. Qin, Silica-coated ZnS quantum dots as fluorescent probes for the sensitive detection of Pb2+ ions, *J. Nanoparticle Res.*, 2014, **16**(12), 2762.
66 M. Gordel-Wójcik, M. Malik, A. Siomra, M. Samoć and M. Nyk, Third-order nonlinear optical properties of aqueous silver sulfide quantum dots, *J. Phys. Chem. Lett.*, 2023, **14**(49), 11117–11124.
67 H. Agbe, N. Raza, D. Dodoo-Arhin, A. Chauhan and R. V. Kumar, H2O2 rejuvenation-mediated synthesis of stable mixed-morphology Ag3PO4 photocatalysts, *Heliyon*, 2018, **4**(4), 1–25.
68 J. Trajić, R. Kostić, N. Romčević, M. Romčević, M. Mitrić, V. Lazović, P. Balaž and D. Stojanović, Raman spectroscopy of ZnS quantum dots, *J. Alloys Compd.*, 2015, **637**, 401–406.
69 S. Dhara, A. Arora, J. Ghatak, K. Chen, C. Liu, L. Chen, Y. Tzeng, B. Raj, Deformation potential dominated phonons in ZnS quantum dots, *arXiv*, preprint arXiv: 0709.1773, 2007.
70 A. Milekhin, N. Yeryukov, L. Sveshnikova, T. Duda, C. Himcinschi, E. Zenkevich and D. Zahn, Resonant Raman scattering of ZnS, ZnO, and ZnS/ZnO core/shell quantum dots, *Appl. Phys. A*, 2012, **107**(2), 275–278.
71 S. Mandal, S. I. Ali, S. Pramanik, A. C. Mandal, Impact of capping agent on structural and optical properties of ZnS nanoparticles, *arXiv*, preprint arXiv: 2304.13420, 2023.
72 B. Choudhury, M. Dey and A. Choudhury, Defect generation, d-d transition, and band gap reduction in Cu-doped TiO2 nanoparticles, *Int. Nano Lett.*, 2013, **3**(1), 25.
73 G. Botelho, J. Andres, L. Gracia, L. S. Matos and E. Longo, Photoluminescence and photocatalytic properties of Ag3PO4 microcrystals: an experimental and theoretical investigation, *ChemPlusChem*, 2016, **81**(2), 202–212.
74 X. Ma, B. Lu, D. Li, R. Shi, C. Pan and Y. Zhu, Origin of photocatalytic activation of silver orthophosphate from first-principles, *J. Phys. Chem. C*, 2011, **115**(11), 4680–4687.
75 S. S. Patil, D. R. Patil, S. K. Apte, M. V. Kulkarni, J. D. Ambekar, C.-J. Park, S. W. Gosavi, S. S. Kolekar and B. B. Kale, Confinement of Ag3PO4 nanoparticles supported by surface plasmon resonance of Ag in glass: efficient nanoscale photocatalyst for solar H2 production from waste H2S, *Appl. Catal. B Environ.*, 2016, **190**, 75–84.
76 I. Kilic, Y. Bayrak, H. Topallar and B. Karagoz, Preparation of Rice Hull-Based Activated Carbon with Ammonium Nitrate, *Asian J. Chem.*, 2013, **25**(9), 4911.

77 B. Ju, F. Yang, K. Huang and Y. Wang, Fabrication, characterization and photocatalytic mechanism of a novel Z-scheme BiOBr/Ag3PO4@ rGO composite for enhanced visible light photocatalytic degradation, *J. Alloys Compd.*, 2020, **815**, 151886.

78 H. Khiar, N. Barka and A. Puga, Metal phosphates for the design of advanced heterogeneous photocatalysts, *Coord. Chem. Rev.*, 2024, **510**, 215814.

79 S. C. Tudu, T. Sarkar, S. Kundu, G. Ghorai, P. K. Sahoo and A. Bhattacharjee, Synthesis and structural characterization of ZnS quantum dots (< 2 nm) vis-à-vis studies on their spectroscopic and dielectric properties, *J. Mater. Sci.: Mater. Electron.*, 2024, **35**(9), 619.

80 L. Ju, Z. Chen, L. Fang, W. Dong, F. Zheng and M. Shen, Sol–gel synthesis and photo-Fenton-like catalytic activity of EuFeO3 nanoparticles, *J. Am. Ceram. Soc.*, 2011, **94**(10), 3418–3424.

81 S.-A. Chang, P.-Y. Wen, T. Wu and Y.-W. Lin, Microwave-assisted synthesis of chalcopyrite/silver phosphate composites with enhanced degradation of Rhodamine B under photo-Fenton process, *Nanomaterials*, 2020, **10**(11), 2300.

82 X. Chen, C. Yu, R. Zhu, N. Li, J. Chen, S. Li, W. Xia, S. Xu, H. Wang and X. Chen, Ag3PO4 deposited on CuBi2O4 to construct Z-scheme photocatalyst with excellent visible-light catalytic performance toward the degradation of diclofenac sodium, *Nanomaterials*, 2019, **9**(7), 959.

83 X. Li, L. Liu, C. Tu, Q. Zhang, X. Yang, D. I. Kolokolov, H. Maltanava, N. Belko, S. Poznyak and M. Samtsov, Zn-BTC MOF as self-template to hierarchical ZnS/NiS2 heterostructure with improved electrochemical performance for hybrid supercapacitor, *Nanomaterials*, 2023, **14**(1), 22.

84 S. Tong, Y. Lin, S. Zhang, J. Nie, C. Luo, Y. Zhang, S. Wu and C. Yang, Performance and mechanisms of photocatalysis of silver phosphate modified by carbon nanosheets doped with both nitrogen and boron for removal of norfloxacin, *J. Environ. Chem. Eng.*, 2023, **11**(5), 110595.

85 Y. Lee, C. H. Lee, T. Nam, S. Lee, I.-K. Oh, J. Y. Yang, D. W. Choi, C. Yoo, H.-j. Kim and W.-H. Kim, Hydrogen barrier performance of sputtered La2O3 films for InGaZnO thin-film transistor, *J. Mater. Sci.*, 2019, **54**(16), 11145–11156.

86 P. Nagajyothi, T. Sreekanth, R. Ramaraghavulu, K. Devarayapalli, K. Yoo, S. P. Vattikuti and J. Shim, Photocatalytic dye degradation and hydrogen production activity of Ag3PO4/g-C3N4 nanocatalyst, *J. Mater. Sci.: Mater. Electron.*, 2019, **30**(16), 14890–14901.

87 X.-F. Tan, S.-S. Zhu, R.-P. Wang, Y.-D. Chen, P.-L. Show, F.-F. Zhang and S.-H. Ho, Role of biochar surface characteristics in the adsorption of aromatic compounds: Pore structure and functional groups, *Chin. Chem. Lett.*, 2021, **32**(10), 2939–2946.

88 W. Zhang, L. Zhou, J. Shi and H. Deng, Synthesis of Ag3PO4/G-C3N4 composite with enhanced photocatalytic performance for the photodegradation of diclofenac under visible light irradiation, *Catalysts*, 2018, **8**(2), 45.

89 K. Kaur, R. Badru, P. P. Singh and S. Kaushal, Photodegradation of organic pollutants using heterojunctions: A review, *J. Environ. Chem. Eng.*, 2020, **8**(2), 103666.

90 C.-C. Wang, C.-K. Lee, M.-D. Lyu and L.-C. Juang, Photocatalytic degradation of CI Basic Violet 10 using TiO2 catalysts supported by Y zeolite: An investigation of the effects of operational parameters, *Dyes Pigm.*, 2008, **76**(3), 817–824.

91 Y. A. Shaban, Enhanced Photocatalytic Removal of Methylene Blue From Seawater Under Natural Sunlight Using Carbon-Modified n-TiO^ sub 2^ Nanoparticles, *Environ. Pollut.*, 2014, **3**(1), 41.

92 Z. Vasiljevic, M. Dojcinovic, J. Vujancevic, I. Jankovic-Castvan, M. Ognjanovic, N. Tadic, S. Stojadinovic, G. Brankovic and M. Nikolic, Photocatalytic degradation of methylene blue under natural sunlight using iron titanate nanoparticles prepared by a modified sol–gel method, *R. Soc. Open Sci.*, 2020, **7**(9), 200708.

93 M. Abdellah, S. Nosier, A. El-Shazly and A. Mubarak, Photocatalytic decolorization of methylene blue using TiO2/UV system enhanced by air sparging, *Alex. Eng. J.*, 2018, **57**(4), 3727–3735.

94 I. Poulios, A. Avranas, E. Rekliti and A. Zouboulis, Photocatalytic oxidation of Auramine O in the presence of semiconducting oxides, *J. Chem. Technol. Biotechnol. Int. Res. Process Environ. Clean Technol.*, 2000, **75**(3), 205–212.

95 A. Bashir, U. Rafique, R. Bashir, S. Jamil, F. Bashir, M. Sultan, M. Mubeen, Z. Mehmood, A. Iqbal and Z. Akhter, Synthesis and comparative evaluation of optical and electrochemical properties of Ni+ 2 and Pr+ 3 ions co-doped mesoporous TiO2 nanoparticles with undoped Titania, *Appl. Nanosci.*, 2021, **11**(9), 2397–2413.

96 I. Poulios and I. Tsachpinis, Photodegradation of the textile dye Reactive Black 5 in the presence of semiconducting oxides, *J. Chem. Technol. Biotechnol. Int. Res. Process Environ. Clean Technol.*, 1999, **74**(4), 349–357.

97 L. Karimi, S. Zohoori and M. E. Yazdanshenas, Photocatalytic degradation of azo dyes in aqueous solutions under UV irradiation using nano-strontium titanate as the nanophotocatalyst, *J. Saudi Chem. Soc.*, 2014, **18**(5), 581–588.

98 H. D. Tran, D. Q. Nguyen, P. T. Do and U. N. Tran, Kinetics of photocatalytic degradation of organic compounds: a mini-review and new approach, *RSC Adv.*, 2023, **13**(25), 16915–16925.

99 L. Y. Kunz, J. Hong, A. R. Riscoe, A. Majumdar and M. Cargnello, Reducing instability in dispersed powder photocatalysis derived from variable dispersion, metallic co-catalyst morphology, and light fluctuations, *J. Photochem. Photobiol.*, 2020, **2**, 100004.

100 A. Amirulsyafiee, M. M. Khan, M. Y. Khan, A. Khan and M. H. Harunsani, La, Zr co-doped Ag3PO4 for enhanced visible-light photocatalytic degradation of dyes and Cr (VI) photoreduction, *Chem. Phys. Impact*, 2022, **5**, 100102.